Study of the reactions $e^+e^- \to K^+K^-\pi^0\pi^0\pi^0$, $e^+e^- \to K^0_S K^\pm\pi^\mp\pi^0\pi^0$, and $e^+e^- \to K^0_S K^\pm\pi^\mp\pi^+\pi^-$ at center-of-mass energies from threshold to 4.5 GeV using initial-state radiation

J. P. Lees, V. Poireau, V. Tisserand, E. Grauges, A. Palano, G. Eigen, D. N. Brown, Yu. G. Kolomensky, M. Fritsch, H. Koch, R. Cheaib, C. Hearty, T. S. Mattison, J. A. McKenna, R. Y. So, V. E. Blinov, A. R. Buzykaev, V. P. Druzhinin, E. A. Kozyrev, E. A. Kravchenko, S. I. Serednyakov, Yu. I. Skovpen, E. P. Solodov, K. Yu. Todyshev, A. J. Lankford, B. Dey, J. W. Gary, O. Long, A. M. Eisner, W. S. Lockman, W. Panduro Vazquez, D. S. Chao, C. H. Cheng, B. Echenard, K. T. Flood, D. G. Hitlin, Y. Li, D. X. Lin, S. Middleton, T. S. Miyashita, P. Ongmongkolkul, J. Oyang, F. C. Porter, M. Röhrken, B. T. Meadows, M. D. Sokoloff, J. G. Smith, S. R. Wagner, D. Bernard, M. Verderi, D. Bettoni, C. Bozzi, R. Calabrese, G. Cibinetto, E. Fioravanti, I. Garzia, E. Luppi, V. Santoro, A. Calcaterra, R. de Sangro, G. Finocchiaro, S. Martellotti, P. Patteri, I. M. Peruzzi, M. Piccolo, M. Rotondo, A. Zallo, S. Passaggio, C. Patrignani, B. J. Shuve, H. M. Lacker, B. Bhuyan, U. Mallik, C. Chen, J. Cochran, S. Prell, A. V. Gritsan, N. Arnaud, M. Davier, F. Le Diberder, A. M. Lutz, G. Wormser, D. J. Lange, D. M. Wright, J. P. Coleman, D. E. Hutchcroft, D. J. Payne, C. Touramanis, A. J. Bevan, F. Di Lodovico, G. Cowan, Sw. Banerjee, D. N. Brown, C. L. Davis, A. G. Denig, W. Gradl, K. Griessinger, A. Hafner, K. R. Schubert, R. J. Barlow, G. D. Lafferty, R. Cenci, A. Jawahery, D. A. Roberts, R. Cowan, S. H. Robertson, R. M. Seddon, N. Neri, F. Palombo, L. Cremaldi, R. Godang, D. J. Summers,[*] G. De Nardo, C. Sciacca, C. P. Jessop, J. M. LoSecco, K. Honscheid, A. Gaz, M. Margoni, G. Simi, F. Simonetto, R. Stroili, S. Akar, E. Ben-Haim, M. Bomben, G. R. Bonneaud, G. Calderini, J. Chauveau, G. Marchiori, J. Ocariz, M. Biasini, E. Manoni, A. Rossi, G. Batignani, S. Bettarini, M. Carpinelli, G. Casarosa, M. Chrzaszcz, F. Forti, M. A. Giorgi, A. Lusiani, B. Oberhof, E. Paoloni, M. Rama, G. Rizzo, J. J. Walsh, L. Zani, A. J. S. Smith, F. Anulli, R. Faccini, F. Ferrarotto, F. Ferroni, A. Pilloni, C. Bünger, S. Dittrich, O. Grünberg, T. Leddig, C. Voß, R. Waldi, T. Adye, F. F. Wilson, S. Emery, G. Vasseur, D. Aston, C. Cartaro, M. R. Convery, M. Ebert, R. C. Field, B. G. Fulsom, M. T. Graham, C. Hast, P. Kim, S. Luitz, D. B. MacFarlane, D. R. Muller, H. Neal, B. N. Ratcliff, A. Roodman, M. K. Sullivan, J. Va'vra, W. J. Wisniewski, M. V. Purohit, J. R. Wilson, S. J. Sekula, H. Ahmed, N. Tasneem, M. Bellis, P. R. Burchat, E. M. T. Puccio, J. A. Ernst, R. Gorodeisky, N. Guttman, D. R. Peimer, A. Soffer, S. M. Spanier, J. L. Ritchie, J. M. Izen, X. C. Lou, F. Bianchi, F. De Mori, A. Filippi, L. Lanceri, L. Vitale, F. Martinez-Vidal, A. Oyanguren, J. Albert, A. Beaulieu, F. U. Bernlochner, G. J. King, R. Kowalewski, T. Lueck, C. Miller, I. M. Nugent, J. M. Roney, R. J. Sobie, T. J. Gershon, P. F. Harrison, T. E. Latham, and S. L. Wu

(The *BABAR* Collaboration)

(Received 23 July 2022; accepted 10 August 2022; published 4 April 2023)

We study the processes $e^+e^- \to K^+K^-\pi^0\pi^0\pi^0\gamma$, $K^0_S K^\pm\pi^\mp\pi^0\pi^0\gamma$, and $K^0_S K^\pm\pi^\mp\pi^+\pi^-\gamma$ in which an energetic photon is radiated from the initial state. The data were collected with the *BABAR* detector at the SLAC National Accelerator Laboratory. About 1200, 2600, and 6000 events, respectively, are selected from a data sample corresponding to an integrated luminosity of 469 fb^{-1}. The invariant mass of the hadronic final state defines the effective e^+e^- center-of-mass energy. The center-of-mass energies range from threshold to 4.5 GeV. From the mass spectra, the first ever measurements of the $e^+e^- \to K^+K^-\pi^0\pi^0\pi^0$, $e^+e^- \to K^0_S K^\pm\pi^\mp\pi^0\pi^0$, and $e^+e^- \to K^0_S K^\pm\pi^\mp\pi^+\pi^-$ cross sections are performed.

[*]Deceased.

The contributions from the intermediate states that include η, ϕ, ρ, $K^*(892)$, and other resonances are presented. We observe the J/ψ and $\psi(2S)$ in most of these final states and measure the corresponding branching fractions, many of them for the first time.

DOI: 10.1103/PhysRevD.107.072001

I. INTRODUCTION

Many precision Standard Model (SM) predictions require taking into account the hadronic vacuum polarization (HVP) terms. At a relatively large momentum transfer, these terms are measured by studying the inclusive hadronic production in e^+e^- annihilation and are relatively well calculated by pQCD. However, in the energy region from the hadronic threshold to about 2 GeV, the inclusive hadronic cross section cannot be measured or calculated reliably, and a sum of exclusive states must be used. It is particularly important for the calculation of the muon anomalous magnetic moment $(g_\mu - 2)$, which is most sensitive to the low-energy region. Despite the large data set of e^+e^- cross sections accumulated in the past years, and the studies performed [1,2], there is still a discrepancy between the SM calculation and the experimental $(g_\mu - 2)$ value. With the latest result of the $(g_\mu - 2)$ experiment at Fermilab [3], this discrepancy increased to 4.2 sigma.

Electron-positron annihilation events with initial-state radiation (ISR) can be used to study processes over a wide range of energies below the nominal e^+e^- center-of-mass (c.m.) energy ($E_{\rm c.m.}$), as proposed in Ref. [4]. The possibility of exploiting ISR to make precise measurements of low-energy cross sections at high-luminosity ϕ and B factories is discussed in Refs. [5–7] and motivates the studies described in this paper. In addition, studies of ISR events at B factories are interesting in their own right because they provide information on resonance spectroscopy for masses up to the charmonium region.

Studies of hadron (h) production in the ISR process $e^+e^- \to h\gamma$ have previously been reported [8–23] by the *BABAR* experiment at SLAC. These studies consider up to seven hadrons with different combinations of particles in the final state. Nevertheless, not all accessible states have yet been measured. For the $e^+e^- \to K\bar{K}3\pi$ process only the $e^+e^- \to K^+K^-\pi^+\pi^-\pi^0$ reaction [12] has been studied, which is dominated by the $\phi(1020)\eta$ and ωK^+K^- intermediate states. Final states with neutral kaons and/or combinations with two or three neutral pions have not been measured. These cross sections could have a sizable value below 2 GeV; however, they have not yet been included in the HVP calculation [1]. A direct measurement of these channels can improve the reliability of the HVP calculation. It is also important to extract the contribution of the intermediate resonances because the total cross section calculation depends on their decay rate to the measured final states.

This paper reports on the *BABAR* data analyses of the $K^+K^-\pi^0\pi^0\pi^0$, $K^0_SK^\pm\pi^\mp\pi^0\pi^0$, and $K^0_SK^\pm\pi^\mp\pi^+\pi^-$ final states produced in e^+e^- collisions in conjunction with an energetic photon, assumed to result from ISR. While the *BABAR* data cover effective c.m. energies up to 10.58 GeV, this analysis is restricted to energies below 4.5 GeV to minimize the backgrounds from $\Upsilon(4S)$ decays. We extract the contributions of intermediate states, including the $\phi(1020)$, $\omega(782)$, $\rho(770)$, η, and $K^*(892)^{\pm,0}$ resonances, and present the corresponding cross sections. Signals for the J/ψ and $\psi(2S)$ states are observed in most of the studied intermediate states, and the corresponding branching fractions are measured.

II. THE *BABAR* DETECTOR AND DATA SET

The data used in this analysis were collected with the *BABAR* detector at the PEP-II2 asymmetric-energy e^+e^- storage ring. The total integrated luminosity used is 468.6 fb^{-1} [24], which includes data collected at the $\Upsilon(4S)$ resonance (424.7 fb^{-1}) and at a c.m. energy 40 MeV below this resonance (43.9 fb^{-1}).

The *BABAR* detector is described in detail elsewhere [25]. Charged particles are reconstructed using the *BABAR* tracking system, which is comprised of the silicon vertex tracker (SVT) and the drift chamber (DCH), both located inside a 1.5 T solenoid. Separation of pions and kaons is accomplished by means of the detector of internally reflected Cherenkov light (DIRC) and energy-loss measurements in the SVT and DCH. Photons and K^0_L mesons are detected in the electromagnetic calorimeter (EMC). Muon identification is provided by the instrumented flux return (IFR).

The ISR events with detection of the ISR photon in the EMC are characterized by good reconstruction efficiency and by well-understood kinematics, demonstrated in the above references. The *BABAR* detector performance [tracking, particle identification (PID), π^0, K^0_S, and K^0_L reconstruction] is well suited to the study of ISR processes.

To evaluate the detector acceptance and efficiency, we have developed a special package of Monte Carlo (MC) simulation programs for radiative processes based on the approach of Kühn and Czyż [26]. Multiple collinear soft-photon emission from the initial e^+e^- state is implemented with the structure function technique [27,28], while additional photon radiation from final-state particles is simulated using the PHOTOS package [29]. The precision of the

radiative simulation is such that it contributes less than 1% to the uncertainty in the measured hadronic cross sections.

We simulate $e^+e^- \to K^+K^-\pi^0\pi^0\pi^0\gamma$ events assuming production through the $\phi(1020)\eta$ intermediate channel, with decay of the ϕ to charged kaons and decay of the η to all its measured decay modes [30]. For the $e^+e^- \to K^0_S K^\pm\pi^\mp\pi^0\pi^0\gamma$ and $e^+e^- \to K^0_S K^\pm\pi^\mp\pi^+\pi^-\gamma$ reactions we use a phase space model for the hadronic states. As was shown in our previous studies, events with hard ISR photon detection are characterized by a weak model dependence, which does not exceed 5%, in the efficiency calculation.

A sample of about 300 000 simulated events is generated for each reaction and is processed through the detector response simulation, based on the GEANT4 package [31]. These events are reconstructed using the same software chain as the data. Most of the experimental events contain additional soft photons due to machine background or interactions in the detector material. Variations in the detector and background conditions are included in the simulation.

For the purpose of background estimation, large samples of events from the main relevant ISR processes ($5\pi\gamma$, $\omega\pi^0\pi^0\gamma$, $K^+K^-\pi^0\pi^0\gamma$, $K^0_S K^\pm\pi^\mp\pi^0\gamma$) are simulated. To evaluate the background from the relevant non-ISR processes, namely, $e^+e^- \to q\bar{q}$ ($q = u, d, s$) and $e^+e^- \to \tau^+\tau^-$, simulated samples with integrated luminosities similar to those of the data are generated using the JetSet [32] and KORALB [33] programs, respectively. The cross sections for the above processes are known with an accuracy slightly better than 10%, which is sufficient for the present purpose.

III. EVENT SELECTION AND KINEMATIC FIT

A relatively clean sample of ISR-related events is selected by requiring that there be charged tracks reconstructed in the DCH, SVT, or both, and some number of photons (sometimes up to 20), with an energy above 0.02 GeV in the EMC. We assume the photon with the highest energy to be the ISR photon, and we require its c.m. energy to be larger than 3 GeV.

The event selections and procedures are based on the methods described in our previous analyses for the $e^+e^- \to \pi^+\pi^-\pi^0\pi^0\pi^0$ [20] and $e^+e^- \to K^0_S K^0_S\pi^+\pi^-$ [18] channels.

We require either exactly two or exactly four tracks in an event with zero total charge that extrapolate to within 0.25 cm of the beam axis and 3.0 cm of the nominal collision point along that axis. If there are two such tracks, we require either that both be identified as kaons or, if only one is identified as a kaon, that a K^0_S candidate be present. We detect K^0_S using $K^0_S \to \pi^+\pi^-$ decays with pions not from the collision region, and we require the decay point to be within 0.2 to 40 cm from the collision point. If there are four tracks from the collision region, we require one of them to be identified as a kaon and require the presence of a K^0_S candidate. We also allow the presence of one extra track to capture the relatively small fraction of signal events that contain a background track. The tracks that satisfy the extrapolation criteria to the collision region are fit to a vertex, which is used as the point of origin in the calculation of the photon direction.

We subject each candidate event to a set of constrained kinematic fits and use the fit results, along with charged-particle identification, to select the final states of interest and evaluate backgrounds from other processes. The kinematic fits make use of the four-momenta and covariance matrices of the initial e^+, e^-, and the set of selected tracks, K^0_S candidates, and photons. The fitted three-momenta of each track, K^0_S, and photon are then used in further calculations.

Excluding the photon with the highest c.m. energy, which is assumed to arise from ISR, we consider all independent sets of six (four) other photons and combine them into three (two) pairs. For each set of six (four) photons, we test all possible independent combinations of three (two) photon pairs. For the next stage we select those combinations in which the di-photon mass of at least two (one) pairs lies within ± 35 MeV/c^2 ($\pm 3\sigma$ of the resolution) of the π^0 mass, m_{π^0} [30].

The selected combinations are subjected to a fit in which the di-photon masses of the two (one) pairs with $|m(\gamma\gamma) - m_{\pi^0}| < 35$ MeV/c^2 are constrained to m_{π^0}. For the signal hypothesis, $e^+e^- \to K^+K^-\pi^0\pi^0\gamma\gamma_{\rm ISR}$, with the constraints due to four-momentum conservation, there are thus six constraints (6C) in the fit. For the $e^+e^- \to K^0_S K^\pm\pi^\mp\pi^0\gamma\gamma_{\rm ISR}$ hypothesis there are five constraints (5C) in the fit. For the $e^+e^- \to K^0_S K^\pm\pi^\mp\pi^+\pi^-\gamma_{\rm ISR}$ hypothesis we use the 4C fit with only four-momentum constraints. The photons in the remaining ("third" or "second") pair are treated as being independent. If all three (two) photon pairs in the combination satisfy $|m(\gamma\gamma) - m_{\pi^0}| < 35$ MeV/c^2, we rotate the combinations, allowing each of the di-photon pairs in turn to be the third (second) pair, i.e., the pair without the m_{π^0} constraint. The combination with the smallest χ^2 is retained, along with the obtained $\chi^2_{2K2\pi^0\gamma\gamma}$ (χ^2_{6C}), $\chi^2_{K^0_S K\pi\pi^0\gamma\gamma}$ (χ^2_{5C}), and $\chi^2_{K^0_S K3\pi}$ (χ^2_{4C}) values and the fitted three-momenta of each particle and photon.

Each retained event is also subjected to a 6C (5C) fit under the $e^+e^- \to K^+K^-\pi^0\pi^0\gamma_{\rm ISR}$ ($e^+e^- \to K^0_S K^\pm\pi^\mp\pi^0\gamma_{\rm ISR}$) background hypothesis, and the smallest values of $\chi^2_{2K2\pi^0}$ and $\chi^2_{K^0_S K\pi\pi^0}$ from all photon combinations are retained. These processes have a comparable cross section to the signal processes and can contribute to the background when two or more background photons are present.

IV. ADDITIONAL SELECTION CRITERIA

The results of the kinematic fits are used to perform the final selection of signal events. We require the tracks to lie

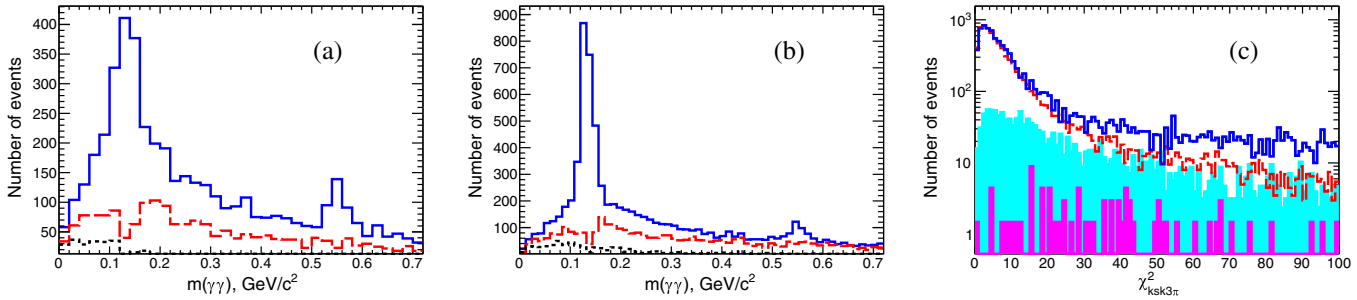

FIG. 1. The $m(\gamma\gamma)$ invariant mass for the third photon pair (a) in the $e^+e^- \to K^+K^-\pi^0\pi^0\gamma\gamma\gamma_{\rm ISR}$ hypothesis and (b) in the $e^+e^- \to K^0_S K^\pm\pi^\mp\pi^0\gamma\gamma\gamma_{\rm ISR}$ hypothesis for the χ^2 signal regions. The dashed histograms are for events from the χ^2 control regions. The dotted histograms are for the remaining $e^+e^- \to K^+K^-\pi^0\pi^0\gamma_{\rm ISR}$ or $e^+e^- \to K^0_S K^\pm\pi^\mp\pi^0\gamma_{\rm ISR}$ backgrounds from simulation. (c) The $\chi^2_{K^0_S K3\pi}$ distribution in the $e^+e^- \to K^0_S K^\pm\pi^\mp\pi^+\pi^-\gamma_{\rm ISR}$ hypothesis for data (solid histogram) and for the MC simulation (dashed). The shaded histogram is for the *uds* backgrounds, and single bins are for the remaining contribution from the $e^+e^- \to K^0_S K^\pm\pi^\mp\gamma_{\rm ISR}$ process.

within the fiducial region of the DCH (0.45–2.40 radians) and to be inconsistent with being a muon. The photon candidates are required to lie within the fiducial region of the EMC (0.35–2.40 radians) and to have an energy larger than 0.035 GeV. A requirement that there be no charged tracks within 1 radian of the ISR photon reduces the $\tau^+\tau^-$ background to a negligible level. A requirement that any extra photons in an event each have an energy below 0.7 GeV slightly reduces the multiphoton background. We use the χ^2 values for the signal selection and for the background evaluation.

We require $\chi^2_{2K2\pi^0\gamma\gamma} < 65$ to select the signal for the $K^+K^-\pi^0\pi^0\pi^0$ events and use events in the control region, $65 < \chi^2_{2K2\pi^0\gamma\gamma} < 130$, for the background estimate. We apply a $\chi^2_{2K2\pi^0} > 30$ condition if these events also satisfy the $K^+K^-\pi^0\pi^0$ background hypothesis. This requirement reduces the contamination due to $K^+K^-\pi^0\pi^0$ events from 30% to about 1%–2% while reducing the signal efficiency by only 5%. Figure 1(a) shows the invariant mass $m(\gamma\gamma)$ of the third photon pair for the $e^+e^- \to K^+K^-\pi^0\pi^0\gamma\gamma\gamma_{\rm ISR}$ hypothesis for the signal and control regions of $\chi^2_{2K2\pi^0\gamma\gamma}$. Clear π^0 and η peaks are visible as well as a relatively smooth background, exceeding the level of events from the χ^2 control region but with a similar shape. Because of the constraint to the best photon pairs, the third photon pair is sometimes formed from photon candidates that are less well measured and have a dip in the distribution, explained in Ref. [20].

Figure 1(b) shows the $m(\gamma\gamma)$ distribution after the $\chi^2_{K^0_S K\pi\pi^0\gamma\gamma} < 70$ requirement has been applied in the $e^+e^- \to K^0_S K^\pm\pi^\mp\pi^0\gamma\gamma\gamma_{\rm ISR}$ hypothesis (solid histogram). The dashed histogram is for the events in the $70 < \chi^2_{K^0_S K\pi\pi^0\gamma\gamma} < 140$ control region, while the dotted histogram is for a remaining $K^0_S K^\pm\pi^\mp\pi^0$ background estimated from the simulation normalized to the known cross section.

Our strategy to extract the signals for the $e^+e^- \to K^+K^-\pi^0\pi^0\pi^0$ and $K^0_S K^\pm\pi^\mp\pi^0\pi^0$ processes is to perform a fit to the π^0 yields in intervals of 0.05 GeV/c^2 in the distributions of the invariant masses $m(K^+K^-2\pi^0\gamma\gamma)$ and $m(K_S K^\pm\pi^\mp\pi^0\gamma\gamma)$. The procedure is described in detail in Ref. [20].

For the $e^+e^- \to K^0_S K^\pm\pi^\mp\pi^+\pi^-\gamma_{\rm ISR}$ process we use the procedure described in Ref. [18], based on the χ^2 distribution study. The signal events are selected by the requirement $\chi^2_{K^0_S K3\pi} < 40$ while the events in the control region, $40 < \chi^2_{K^0_S K3\pi} < 80$, are used for the background evaluation. Figure 1(c) shows the $\chi^2_{K^0_S K3\pi}$ distribution for data (solid histogram) in comparison with the simulation (dashed), normalized to the first five bins where the contribution from the background is small. The non-ISR background is shown by the shaded histogram (see next section) while the remaining $K^0_S K^\pm\pi^\mp$ events are at a negligible level [individual (pink) bins].

V. DETECTION EFFICIENCY

A. Number of signal events in simulation

The selection procedure applied to the data is also applied to the MC-simulated events. Figure 2 shows the two-photon and three-pion invariant mass distributions, which are used to extract the number of signal events.

The π^0 signal for the simulation is not Gaussian because of the photon pair selection, which was described in the previous section. It also includes a combinatoric background arising from the combination of background photons, included in the simulation, with the photons from the signal reactions. This combinatoric background can be subtracted using events from the χ^2 control region, shown by the dashed histogram in Fig. 2(a). The solid histogram in Fig. 2(a) corresponds to the two-photon mass distribution obtained from the χ^2 signal region for MC simulation of the $\phi\eta$ final state after the combinatoric background subtraction. The background is subtracted assuming a scale factor, which is varied to estimate the uncertainty in its contribution. The signal yield is then

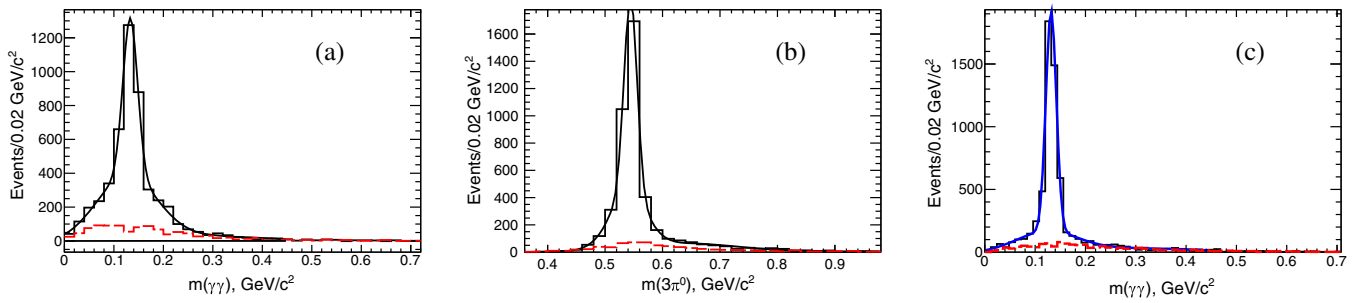

FIG. 2. (a) Third photon pair $m(\gamma\gamma)$ invariant mass for the MC simulated $\phi\eta$ events after applied selections and background subtraction (solid histogram). The dashed histogram shows the contribution of the subtracted events from the χ^2 control region. The curve is for the three-Gaussian fit to the π^0 signal. (b) Background-subtracted $\pi^0\pi^0\pi^0$ invariant mass distribution (solid histogram) for the MC simulated $\phi\eta$ final state, and the events from the χ^2 control region (dashed histogram). The solid curve is fit to the η signal. (c) Background-subtracted second photon pair invariant mass (solid histogram) for the $K^0_S K^\pm\pi^\mp\pi^0\pi^0$ final state with the three-Gaussian fit function. The dashed histogram shows the contribution from the χ^2 control region.

extracted by fitting the π^0 peak of this distribution with a sum of three Gaussian functions for the signal plus a second-order polynomial function to account for a residual combinatoric background. If a scale factor 1.5 is used, the background level becomes negligible, and we can determine and fix all parameters for the signal function. If we then change the scale factor to 1.0 or to 0.0 in the fit, the fitted signal yield does not change by more than 3%. The result, for a scale factor of 1.0, is shown by the smooth solid curve in Fig. 2(a). We apply a similar fitting procedure in every 0.05 GeV/c^2 interval of the $m(K^+K^-3\pi^0)$ invariant mass distribution.

As a cross-check, for the $\phi\eta$ events, we determine the number of events by fitting the η signal from $\eta \to \pi^0\pi^0\pi^0$ decay: the simulated distribution is shown in Fig. 2(b) after combinatoric background subtraction with a scale factor 1.0. The fit functions are the sum of three Gaussian functions and a polynomial for the combinatoric background. No difference in the number of events is observed. The $K^+K^-\pi^0\pi^0\pi^0$ mass distribution is also obtained in every 0.05 GeV/c^2 interval.

The same approach is used for the $K^0_S K^\pm\pi^\mp\pi^0\pi^0$ final state. Figure 2(c) shows the second photon pair invariant mass distribution after combinatorial background subtraction with a scale factor of 1.0. The dashed histogram shows the level of this background. The curve shows the fit function used to determine the number of events.

For the $K^0_S K\pi\pi^+\pi^-$ final state we use simulated events in the χ^2 signal region for the efficiency evaluation. There is no combinatorial background for this final state.

B. Efficiency evaluation

The mass-dependent detection efficiency is obtained by dividing the number of fitted MC events in each 0.05 GeV/c^2 mass interval by the number generated in the same interval. We determine that the total efficiency does not change by more than 5% because of variations of the functions used to extract the number of events or the use of different background subtraction procedures. This value is taken as an estimate of the systematic uncertainty in the efficiency associated with the simulation model used and with the fit procedure. We obtain the efficiency in each 0.05 GeV/c^2 mass interval for the $K^+K^-\pi^0\pi^0\pi^0$ final state and fit the result with a third-order polynomial function, shown in Fig. 3(a). Although the signal simulation accounts for all η decay modes, the efficiency calculation considers only the

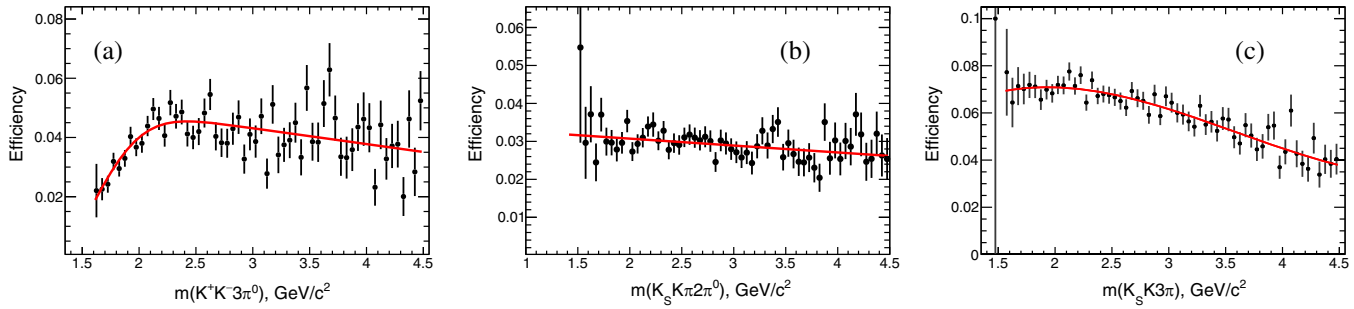

FIG. 3. Hadronic invariant-mass-dependent reconstruction efficiency for (a) the $e^+e^- \to K^+K^-\pi^0\pi^0\pi^0\gamma_{\rm ISR}$ events, (b) the $e^+e^- \to K^0_S K^\pm\pi^\mp\pi^0\pi^0\gamma_{\rm ISR}$ events, and (c) the $e^+e^- \to K^0_S K^\pm\pi^\mp\pi^+\pi^-\gamma_{\rm ISR}$ events. The curves show the fit results, which are used in the cross section calculation.

$\eta \to \pi^0\pi^0\pi^0$ decay mode. From Fig. 3(b) it is seen that the reconstruction efficiency for the $K^0_S K\pi\pi^0\pi^0$ final state is about 3%, roughly independent of mass. The result of the linear fit is used for the cross section calculation. Figure 3(c) shows the detection efficiency for the $K^0_S K\pi\pi^+\pi^-$ final state with the fit function used for the cross section calculation.

This efficiency estimate takes into account the geometrical acceptance of the detector for the final-state photons and the charged pions and kaons, the inefficiency of the detector subsystems, and the event loss due to additional soft-photon emission from the initial and final states. Corrections to the efficiency that account for data-MC differences are discussed below.

VI. CROSS SECTION CALCULATIONS

A. Number of signal events

The solid histograms in Fig. 1 show the $m(\gamma\gamma)$ invariant mass distributions for two photons for data in the χ^2 signal region for the ISR processes $e^+e^- \to K^+K^-\pi^0\pi^0\gamma\gamma$ (a) and $e^+e^- \to K^0_S K^\pm\pi^\mp\pi^0\gamma\gamma$ (b), while the dashed histograms show the distribution of data from the χ^2 control region. The dotted histograms are the estimated contribution from the remaining background from other ISR-related processes using simulation. No evidence for a peaking background is seen in either of the two background distributions. The background includes not only the combinatorial part as modeled in MC simulation but also a general background from B hadron decays and other processes at the nominal c.m. energy. We subtract the background evaluated using the χ^2 control region with the scale factor 1.0 and fit the data with a combination of three Gaussian signal functions and a background function, taken to be a third-order polynomial. All parameters of the Gaussians are fixed to values taken from simulation fits except the number of events. The fit is performed in the $m(\gamma\gamma)$ mass range from 0.0 to 0.45 GeV/c^2. In total 1230 ± 168 and 2658 ± 65 events are obtained for the $K^+K^-\pi^0\pi^0\pi^0$ and $K^0_S K^\pm\pi^\mp\pi^0\pi^0$ channels, respectively. Note that these numbers include a relatively small peaking background component, due to $q\bar{q}$ events, which is discussed in Sec. VI B. The same fit is applied to the corresponding $m(\gamma\gamma)$ distribution in each 0.05 GeV/c^2 interval in the $K^+K^-\pi^0\pi^0\pi^0\gamma\gamma$ and $K^0_S K^\pm\pi^\mp\pi^0\gamma\gamma$ invariant mass. The resulting numbers of $K^+K^-\pi^0\pi^0\pi^0$ and $K^0_S K^\pm\pi^\mp\pi^0\pi^0$ event candidates, including the peaking $q\bar{q}$ background, are shown as a function of hadronic mass by the points in Figs. 4(a) and 4(b). We vary the fitting procedure by releasing the resolution and the position of the main Gaussian function or varying the scale factor. A variation of about 7% in the number of events is taken as the estimate of the systematic uncertainty.

For the $K^0_S K^\pm\pi^\mp\pi^+\pi^-$ final state we obtain 6582 event candidates from the signal and 737 events from the control region in the χ^2 distribution of Fig. 1(c), shown by solid and dashed histograms in Fig. 4(c).

B. Peaking background

The major background producing signal-like events following the application of the selection criteria of Sec. IV is from non-ISR $q\bar{q}$ events, the most important channels being $e^+e^- \to K^+K^-\pi^0\pi^0\pi^0\pi^0$, $e^+e^- \to K^0_S K^\pm\pi^\mp\pi^0\pi^0\pi^0$, and $e^+e^- \to K^0_S K^\pm\pi^\mp\pi^+\pi^-\pi^0$ in which one of the neutral pions decays asymmetrically, yielding a high energy photon that mimics an ISR photon. We apply all our selection criteria and fit procedures to the non-ISR light quark $q\bar{q}$ (uds) simulation. Indeed, we observe a π^0 peak in the $m(\gamma\gamma)$ invariant mass distributions for the $K^+K^-\pi^0\pi^0\pi^0\gamma\gamma$ and $K^0_S K^\pm\pi^\mp\pi^0\gamma\gamma$ candidate events. Also we have 459 uds events in the χ^2 signal region for the $K^0_S K^\pm\pi^\mp\pi^+\pi^-$ final state, shown by the shaded histogram in Fig. 4(c).

To normalize the uds simulation, we form the di-photon invariant mass distribution of the ISR candidate with each of the other photons in the event. A π^0 peak is observed, with approximately the same number of events in data and simulation, leading to a normalization factor of 1.0 ± 0.1. The resulting uds background is shown in Figs. 4(a) and 4(b) by squares: the uds background is negligible

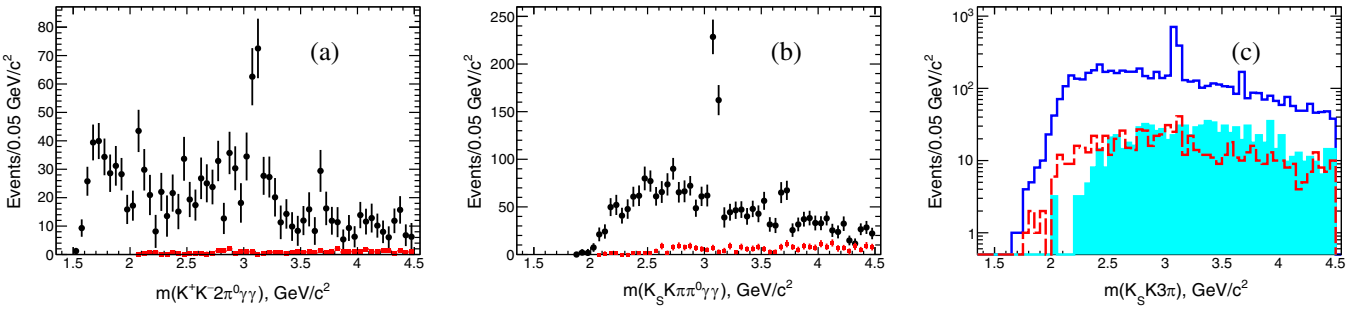

FIG. 4. Number of events determined from the π^0 fit vs the hadronic invariant mass for the (a) $e^+e^- \to K^+K^-\pi^0\pi^0\pi^0$ and (b) $e^+e^- \to K^0_S K\pi\pi^0\pi^0$ reactions. The contributions from uds events are shown by (red) squares. (c) Number of $e^+e^- \to K^0_S K\pi\pi^+\pi^-$ events in the χ^2 signal (solid histogram) and control (dashed) regions. The shaded histogram shows the contribution from the uds events.

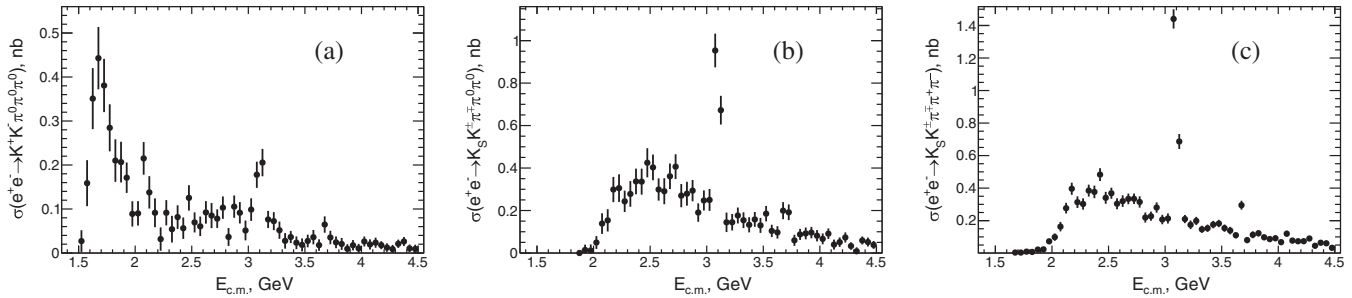

FIG. 5. Measured (a) $e^+e^- \to K^+K^-\pi^0\pi^0\pi^0$, (b) $e^+e^- \to K^0_S K^\pm\pi^\mp\pi^0\pi^0$, and (c) $e^+e^- \to K^0_S K^\pm\pi^\mp\pi^+\pi^-$ cross sections. The uncertainties are statistical only.

below 2 GeV/c^2 and increases slightly with energy from 2 to 4.5 GeV/c^2. We subtract this background for the cross section calculation.

C. Cross section evaluation

The $e^+e^- \to$ hadrons Born cross section is determined from

$$\sigma(\mathrm{had})(\mathrm{E_{c.m.}}) = \frac{\mathrm{dN_{had}}(\mathrm{E_{c.m.}})}{d\mathcal{L}(\mathrm{E_{c.m.}})\epsilon^{\mathrm{corr}}_{\mathrm{had}}\epsilon^{\mathrm{MC}}_{\mathrm{had}}(\mathrm{E_{c.m.}})(1+\delta_{\mathrm{R}})}, \qquad (1)$$

where $E_{\mathrm{c.m.}}$ is the invariant mass of the hadronic system, dN_{had} is the background-subtracted number of selected signal events in the interval $dE_{\mathrm{c.m.}}$, and $\epsilon^{\mathrm{MC}}_{\mathrm{had}}(E_{\mathrm{c.m.}})$ is the corresponding detection efficiency from simulation. The factor $\epsilon^{\mathrm{corr}}_{\mathrm{had}}$ accounts for the difference between data and simulation in the tracking ($1.0\% \pm 1.0\%$/per track) [10] and π^0 ($3.0\% \pm 1.0\%$ per pion) [19] reconstruction efficiencies. The ISR differential luminosity $d\mathcal{L}$ is calculated using the total integrated *BABAR* luminosity of 469 fb^{-1} [9]. The initial- and final-state soft-photon emission is accounted for by the radiative correction factor $(1+\delta_{\mathrm{R}})$, which lies within 1% of unity for our selection criteria. The cross section results contain the effect of vacuum polarization because this effect is not accounted for in the luminosity calculation.

Our results for the $e^+e^- \to K^+K^-\pi^0\pi^0\pi^0$ cross section are shown in Fig. 5(a). The cross section exhibits a structure around 1.7 GeV with a peak value of about 0.4 nb, followed by a monotonic decrease toward higher energies, perturbed by the J/ψ and $\psi(2S)$ signals. Because we present our data in bins of width 0.05 GeV/c^2, compatible with the experimental resolution, we do not apply an unfolding procedure to the data.

Figure 5 also shows the $e^+e^- \to K^0_S K^\pm\pi^\mp\pi^0\pi^0$ (b) and $e^+e^- \to K^0_S K^\pm\pi^\mp\pi^+\pi^-$ (c) cross sections. Some possible structures are seen above 2 GeV, and more prominent signals from J/ψ and $\psi(2S)$ are observed. Numerical values for the cross sections are presented in Tables III–V. The J/ψ region is discussed later.

Our results represent the first measurements of these cross sections.

D. Summary of systematic studies

The systematic uncertainties, presented in the previous sections, are summarized in Table I, along with the corrections that are applied to the measurements.

The three corrections applied to the cross sections sum up to 12.5%, 10.5%, and 6.5% for the $e^+e^- \to K^+K^-\pi^0\pi^0\pi^0$, $e^+e^- \to K^0_S K^\pm\pi^\mp\pi^0\pi^0$, and $e^+e^- \to K^0_S K^\pm\pi^\mp\pi^+\pi^-$ cross sections, respectively, with the corresponding systematic uncertainties estimated as 10%, 10%, and 8%. The largest systematic uncertainty arises from the fitting and background subtraction procedures of the π^0 signal. This is estimated by varying the background levels and the parameters of the functions used.

VII. INTERMEDIATE STRUCTURES IN THE $K^+K^-\pi^0\pi^0\pi^0$ FINAL STATE

As we assumed from the beginning, the $e^+e^- \to K^+K^-\pi^0\pi^0\pi^0$ reaction has a significant contribution from the $\phi(1020)\eta$ intermediate state. Indeed, Fig. 6(a) exhibits a clear η meson peak in the three-pion invariant mass $m(3\pi^0)$.

TABLE I. Summary of correction factors and systematic uncertainties in the $e^+e^- \to K^+K^-\pi^0\pi^0\pi^0 (K^0_S K^\pm\pi^\mp\pi^0\pi^0$, $K^0_S K^\pm\pi^\mp\pi^+\pi^-)$ cross section measurements. The total uncertainly is computed assuming no correlations.

Source	Correction (%)	Uncertainty (%)
Luminosity	⋯	1
MC-data difference in:		
ISR photon efficiency	+1.5	1
Track losses, PID	+2(3, 5)	2(3, 3)
π^0 losses	+9(6, 0)	4(2, 0)
χ^2 cut uncertainty	⋯	3
Fit and background subtraction	⋯	7(7, 0)
Radiative corrections accuracy	⋯	1
Efficiency from MC (model-fit-dependent)	⋯	5
Total	+12.5(10.5, 6.5)	10(10, 8)

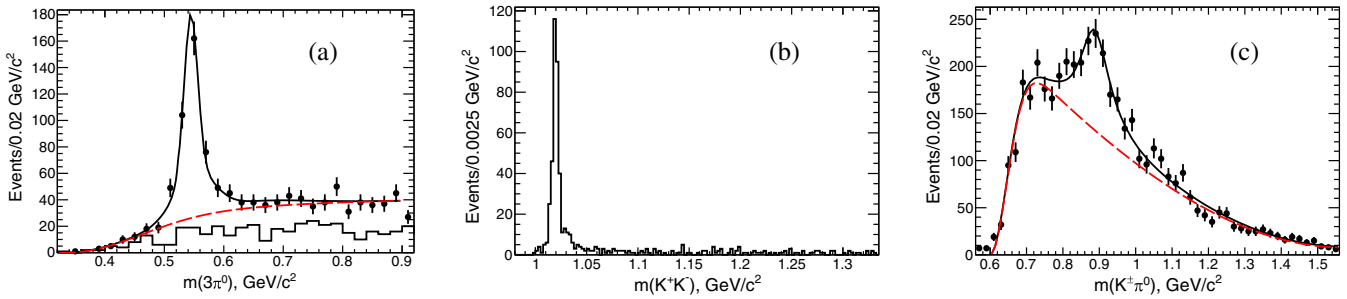

FIG. 6. For the $e^+e^- \to K^+K^-\pi^0\pi^0\pi^0$ reaction: (a) $m(3\pi^0)$ invariant mass distribution for the χ^2 signal (dots) and control (histogram) regions. The curve shows a fit to the $\eta \to \pi^0\pi^0\pi^0$ signal. The dashed line shows the combinatorial background. (b) The $m(K^+K^-)$ invariant mass distribution for events with $m(3\pi^0) < 0.7$ from (a). (c) The $m(K^\pm\pi^0)$ invariant mass distribution (six entries/event). The curve shows a fit to the $K^*(892)$ signal.

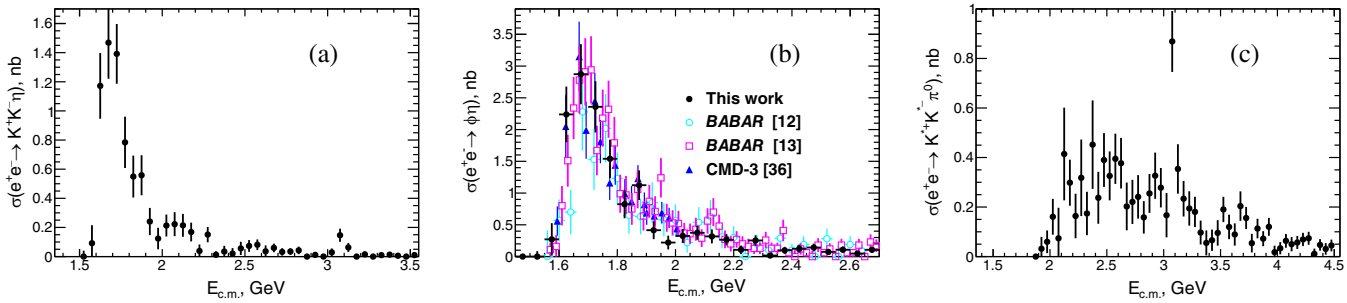

FIG. 7. Measured (a) $e^+e^- \to K^+K^-\eta$, (b) $e^+e^- \to \phi\eta$, and (c) $e^+e^- \to K^{*+}K^{*-}\pi^0$ cross sections. The uncertainties are statistical only.

The histogram shows a background contribution from the χ^2 control region. The fit, with a two-Gaussian function for the signal and a polynomial function for the background, yields 353 ± 28 events for the $K^+K^-\eta$ intermediate state. The cross section for the $e^+e^- \to K^+K^-\eta$ reaction is shown in Fig. 7(a) and listed in Table VI, accounting for the $\eta \to \pi^0\pi^0\pi^0$ branching ratio. If we restrict the three-pion mass by the requirement $m(3\pi^0) < 0.7$ GeV/c^2, the $m(K^+K^-)$ invariant mass exhibits a $\phi(1020)$ resonance, shown in Fig. 6(b). With the $m(K^+K^-) < 1.05$ GeV/c^2 selection we determine the cross section for the $e^+e^- \to \phi\eta$ process, shown as solid dots in Fig. 7(b), in comparison with other measurements by *BABAR* [12] (open squares), *BABAR* [13] (open circles), and CMD-3 [34] (triangles). The decay rates $\phi \to K^+K^-$ and $\eta \to \pi^0\pi^0\pi^0$ are taken into account. The result is listed in Table VII.

Figure 6(c) shows (dots) the $m(K^\pm\pi^0)$ invariant mass (six entries/event). This distribution exhibits a clear signal from $K^*(892)^\pm$. We fit this distribution with a Breit-Wigner (BW) function and combinatorial background, yielding 1506 ± 84 signal events. We conclude that the $K^{*\pm}$ signal arises from $e^+e^- \to K^{*+}K^{*-}\pi^0$ production, and we calculate the corresponding cross section, which is shown in

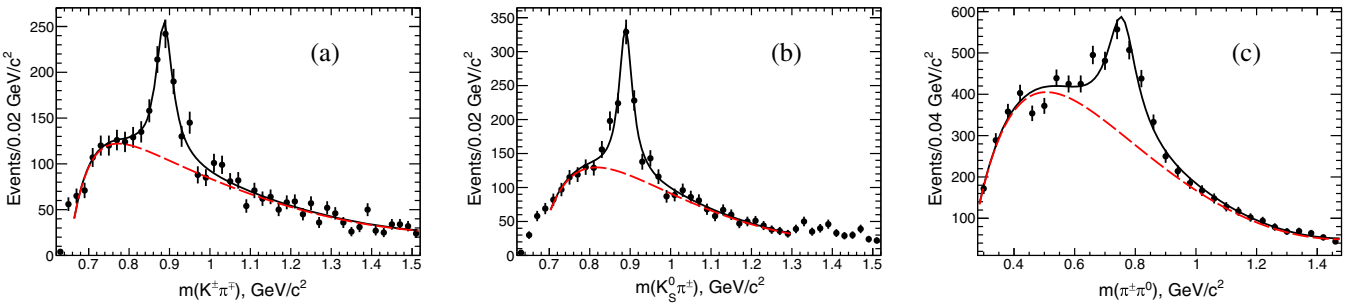

FIG. 8. (a) $m(K^\pm\pi^\mp)$, (b) $m(K^0_S\pi^\pm)$, and (c) $m(\pi^\pm\pi^0)$ invariant mass distributions for the $K^0_SK^\pm\pi^\mp\pi^0\pi^0$ events. The curves show the fit to the $K^*(892)$ and $\rho(770)$ signals with the combinatoric background contribution shown by the dashed curves.

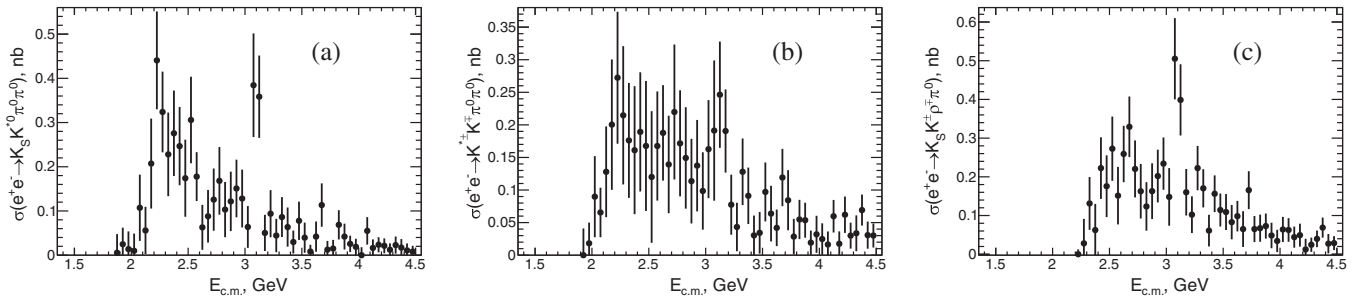

FIG. 9. Measured (a) $e^+e^- \to K^0_S K^{*0}\pi^0\pi^0$, (b) $e^+e^- \to K^{*\pm}K^{\mp}\pi^0\pi^0$, and (c) $e^+e^- \to K^0_S K^{\pm}\rho^{\mp}\pi^0$ cross sections. The uncertainties are statistical only.

Fig. 7(c) and tabulated in Table VIII. The cross section accounts for the 50% branching ratio of $K^{*\pm} \to K^{\pm}\pi^0$. The final state with only one K^* does not exceed 10%, which is within the statistical uncertainty.

VIII. INTERMEDIATE STRUCTURES IN THE $K^0_S K^{\pm}\pi^{\mp}\pi^0\pi^0$ FINAL STATE

Figures 8(a) and 8(b) show the $m(K^{\pm}\pi^{\mp})$ and $m(K^0_S\pi^{\pm})$ invariant mass distributions for the $K^0_S K^{\pm}\pi^{\mp}\pi^0\pi^0$ final state. Clear signals from $K^*(892)^0$ and $K^*(892)^{\pm}$ are seen. A fit based on a BW and a combinatorial background function yields 593 ± 53 and 674 ± 55 events, respectively. We perform similar fits for every 0.05 GeV/c^2 interval in the hadronic invariant mass and calculate the corresponding cross sections, shown in Figs. 9(a) and 9(b) and listed in Tables IX and X. They are very similar in shape and values. We have extracted the correlated production yields of the K^* mesons, with 115 ± 45 events for the $e^+e^- \to K^{*0}\bar{K}^{*0}\pi^0$ and 339 ± 45 events for the $e^+e^- \to K^{*+}K^{*-}\pi^0$ reactions. The corresponding cross section for the latter is in agreement with that in Fig. 7(c).

Figure 8(c) shows the $m(\pi^{\pm}\pi^0)$ invariant mass distribution. A clear peak from the $\rho(770)$ is visible. A fit based on a BW and a combinatorial background function yields 1535 ± 84 $e^+e^- \to K^0_S K^{\pm}\rho^{\mp}\pi^0$ events. The corresponding cross section is shown in Fig. 9(c) and listed in Table XI. A correlated production study yields 194 ± 62 and 170 ± 59 events for the $e^+e^- \to K^0_S K^{*\pm}\rho^{\mp}$ and $e^+e^- \to K^{*0}K^{\pm}\rho^{\mp}$ reactions, respectively. The number of events is too low to present the cross sections for these reactions.

IX. INTERMEDIATE STRUCTURES IN THE $K^0_S K^{\pm}\pi^{\mp}\pi^+\pi^-$ FINAL STATE

A. States with K^{*0}, $K^{*\pm}$, or $\rho^0(770)$

The $e^+e^- \to K^0_S K^{\pm}\pi^{\mp}\pi^+\pi^-$ reaction is dominated by $K^*(892)$ in the intermediate states. Figures 10(a) and 10(b) show the $m(K^{\pm}\pi^{\mp})$ and $m(K^0_S\pi^{\pm})$ invariant mass with fit functions yielding 2587 ± 86 of $K^*(892)^0$ and 2407 ± 85 of $K^*(892)^{\pm}$ events. The $m(\pi^+\pi^-)$ invariant mass, shown in Fig. 10(c), exhibits a large fraction of events with $\rho(770)$ in the intermediate state, with a fit yielding 3583 ± 140 such events. The sum of the three yields exceeds the total number of the $K^0_S K^{\pm}\pi^{\mp}\pi^+\pi^-$ events, indicating a correlated production of the above resonances. Because of the many possible correlations, we do not extract the cross sections for the intermediate states. Figure 11 shows the mass dependence for the number of $K^0_S K^{\pm}\pi^{\mp}\pi^+\pi^-$ events that include (a) K^{*0}, (b) $K^{*\pm}$, or (c) $\rho^0(770)$. All distributions demonstrate relatively large signals from the J/ψ and $\psi(2S)$ resonances. The uds non-ISR background events are shown by (red) squares. The mass-dependent behavior for the $K^*(892)$ production is very close to that for the total $e^+e^- \to K^0_S K^{\pm}\pi^{\mp}\pi^+\pi^-$ cross section in Fig. 5(c). By studying the correlations we estimate that about 40% of events, 1024 ± 77, correspond to the $e^+e^- \to K^{*0}K^{*\pm}\pi^{\mp}$

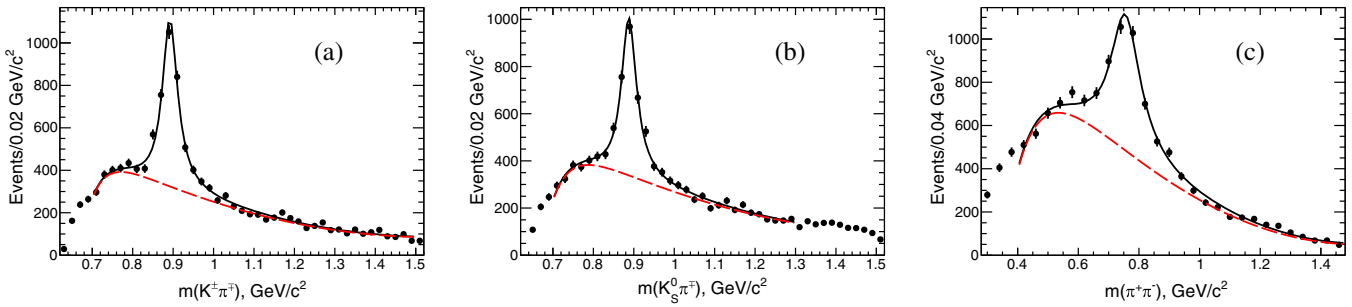

FIG. 10. (a) $m(K^{\pm}\pi^{\mp})$, (b) $m(K^0_S\pi^{\pm})$, and (c) $m(\pi^{\pm}\pi^0)$ invariant mass distributions for the $K^0_S K^{\pm}\pi^{\mp}\pi^+\pi^-$ events. The curves show fits to (a, b) the $K^*(892)$ signal and to (c) the $\rho(770)$ signal. The dashed curves indicate the combinatoric background.

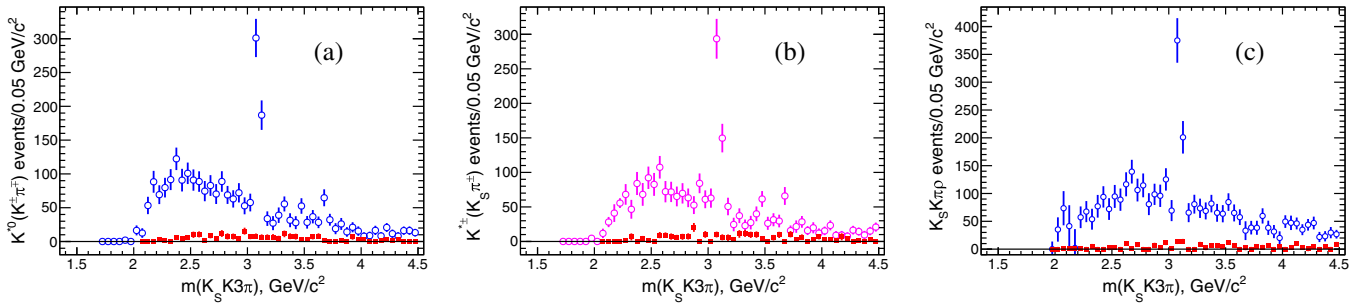

FIG. 11. Observed mass dependence for the (a) $e^+e^- \to K^0_S K^{*0}\pi^+\pi^-$, (b) $e^+e^- \to K^{*\pm}K^{\mp}\pi^+\pi^-$, and (c) $e^+e^- \to K^0_S K^{\pm}\rho^0\pi^{\mp}$ reactions. The contribution from the *uds* reaction is shown by squares.

reaction. The mass-dependent number of ρ^0 events exhibits some structure, as discussed below. We estimate that 165 ± 110 of ρ^0 events are correlated with the K^{*0} production and 402 ± 116 events are correlated with the $K^{*\pm}$ production.

B. The $e^+e^- \to f_1(1285)\rho$ reaction

Figure 12(a) shows the $m(K^0_S K^{\pm}\pi^{\mp})$ invariant mass from the $e^+e^- \to K^0_S K^{\pm}\pi^{\mp}\pi^+\pi^-$ reaction with two entries per event. We fit the observed peak with a BW function and the combinatorial background with a third-order polynomial and obtain $m = 1.283 \pm 0.002$ GeV/c^2 for the mass and $\Gamma = 0.022 \pm 0.007$ GeV for the width of the resonance. This is interpreted as $f_1(1285)$ production in the $e^+e^- \to f_1(1285)\rho$ reaction. The presence of $\rho^0(770)$ is seen from the scatter plot of $m(\pi^+\pi^-)$ vs $m(K^0_S K^{\pm}\pi^{\mp})$ shown in Fig. 12(b). The $e^+e^- \to f_1(1285)\pi^+\pi^-$ cross section was measured for the first time by *BABAR* [12], where $f_1(1285)$ was observed in the $f_1(1285) \to \eta\pi^+\pi^-$ decay. We extract the number of $f_1(1285)$ events in 0.1 GeV/c^2 bins of the $K^0_S K\pi\pi^+\pi^-$ invariant mass and calculate the energy-dependent cross section for the $e^+e^- \to f_1(1285)\pi^+\pi^-$ reaction shown as dots in Fig. 13 and listed in Table XII. The number of events is corrected by a factor of 3 for the missing kaonic channels and for the branching fraction of $f_1(1285) \to K\bar{K}\pi$, 0.09, taken from Ref. [30]. Using our results and data and the BW function suggested in Ref. [12], we perform a combined fit and obtain the following parameters for the resonance:

$$\sigma_0 = 0.85 \pm 0.12 \text{ nb},$$
$$m = 2.09 \pm 0.03 \text{ GeV}/c^2,$$
$$\Gamma = 0.50 \pm 0.06 \text{ GeV}/c^2,$$

consistent with that in Ref. [12] with better statistical accuracy. This structure is included in the PDG [30] as the $\rho(2150)$ resonance.

C. Structures at 2.4 GeV

In the cross section for the $e^+e^- \to K^0_S K^{\pm}\pi^{\mp}\pi^+\pi^-$ reaction in Fig. 5(c), some structures are seen above 2 GeV. We plot the number of signal events of Fig. 4(c) in bins of width 0.02 GeV/c^2 in the hadronic invariant mass and show them in Fig. 14(a). An indication of a bump is seen around 2.4 GeV/c^2. We fit this region with a BW function and a polynomial function for a nonresonant background and obtain the following parameters:

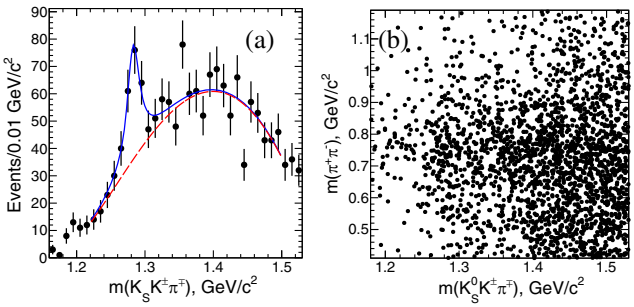

FIG. 12. (a) $m(K^0_S K^{\pm}\pi^{\mp})$ invariant mass distribution. The solid curve is the fit to the $f_1(1285)$ signal with the combinatorial background, shown by the dashed curve. (b) Scatter plot for the $m(\pi^+\pi^-)$ vs $m(K^0_S K^{\pm}\pi^{\mp})$ invariant mass.

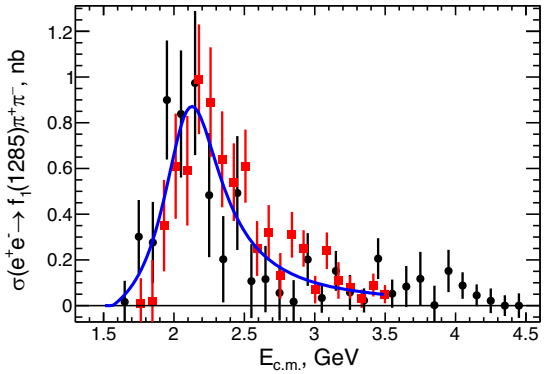

FIG. 13. Measured $e^+e^- \to f_1(1285)\pi^+\pi^-$ cross section from the present analysis (dots) in comparison with previous measurements (squares) [12]. The solid curve is the fit explained in the text.

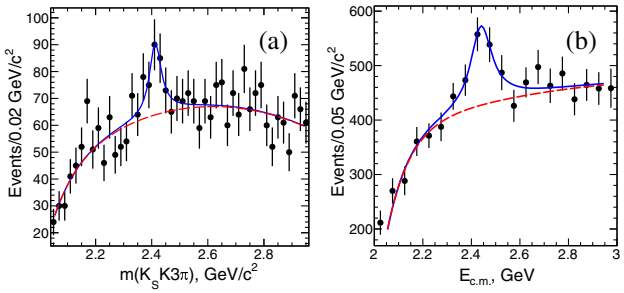

FIG. 14. (a) $m(K^0_S K3\pi)$ invariant mass distribution. The solid curve shows the fit to the $X(2400)$ signal with a combinatorial background, shown by the dashed curve. (b) Sum of events from the $e^+e^- \to K^0_S K^\pm\pi^\mp\pi^+\pi^-$, $e^+e^- \to K^+K^-\pi^+\pi^-\pi^0$, and $e^+e^- \to \pi^+\pi^-\pi^+\pi^-\pi^0\pi^0\pi^0$ reactions. The fit is the same as for (a).

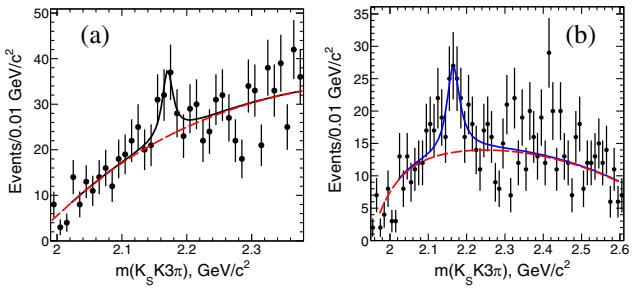

FIG. 15. (a) $m(K^0_S K3\pi)$ invariant mass distribution around 2.17 GeV/c^2. The curves are fits to the $\phi(2170)$ signal with a combinatorial background. (b) Same as (a) with the additional requirement $m(\pi^+\pi^-) < 0.7$ GeV/c^2. The solid curve is a fit to the $\phi(2170)$ signal, with the combinatorial background shown by the dashed curve.

$$N = 108 \pm 50 \text{ events},$$
$$m = 2.41 \pm 0.01 \text{ GeV}/c^2,$$
$$\Gamma = 0.051 \pm 0.027 \text{ GeV}/c^2.$$

The significance of the signal is 2.9 standard deviations. Similar behavior with less statistical significance is seen in the $e^+e^- \to K^0_S K^\pm\pi^\mp\pi^0\pi^0$ and $e^+e^- \to K^+K^-\pi^0\pi^0\pi^0$ reactions of Figs. 5(a) and 5(b). We examine our other measurements of the cross sections, and similar indications are seen in the $e^+e^- \to K^+K^-\pi^+\pi^-\pi^0$ reaction [12] and in the $e^+e^- \to \pi^+\pi^-\pi^+\pi^-\pi^0\pi^0\pi^0$ reaction [22]. We combine events from these two reactions with that from Fig. 14(a) in 0.05 MeV bins and perform a similar fit, shown in Fig. 14(b). The signal has 3.5 standard deviations significance with the following parameters:

$$N = 487 \pm 251 \text{ events},$$
$$m = 2.44 \pm 0.02 \text{ GeV}/c^2,$$
$$\Gamma = 0.107 \pm 0.049 \text{ GeV}/c^2.$$

This resonance structure was also seen and discussed by *BABAR* [15] in the $e^+e^- \to K^+K^- f_0(980)$ [and not well seen in $e^+e^- \to \phi f_0(980)$] reaction and was studied by the Belle [35] experiment. Later, Shen and Yuan [36] performed a fit to the structure called X(2400) using the combined data of the Belle and *BABAR* experiments. The mass and the width were determined to be 2436 ± 26 MeV/c^2 and 121 ± 35 MeV, respectively. However, its statistical significance was less than 3σ, and the structure can be explained as a threshold behavior of the $e^+e^- \to \phi f_0(1370)$ reaction.

D. Structure at 2.17 GeV

Figure 14(a) also shows a few points in the region of the $\phi(2170)$ [30] resonance where the data lie above the fit. We investigate this excess further. Figure 15(a) shows the same plot with a 0.01 GeV/c^2 bin width for the $m(K^0_S K3\pi)$ invariant mass. A signal peak is seen, and a fit with a BW and a polynomial function yields a result with about 2.5σ significance. We apply additional selection criteria to try to increase the possible signal. Figure 15(b) shows a similar plot with the additional requirement $m(\pi^+\pi^-) < 0.7$ GeV/c^2, which decreases the contribution from $\rho(770)$ in this region. The signal is more prominent and the fit gives

$$N = 86 \pm 34 \text{ events},$$
$$m = 2.164 \pm 0.006 \text{ GeV}/c^2,$$
$$\Gamma = 0.041 \pm 0.020 \text{ GeV}/c^2,$$

with 3.9σ significance. Additional selections that enlarge the contribution from K^{*0} or (and) $K^{*\pm}$ do not increase the signal. The observed signal in the $K^0_S K^\pm\pi^\mp\pi^+\pi^-$ final state could be one more decay channel for the $\phi(2170)$ resonance.

X. THE J/ψ REGION

Figure 16 shows an expanded view of the J/ψ mass region from Fig. 4 for the selected data sample. Signals from J/ψ and $\psi(2S)$ to $K^+K^-\pi^0\pi^0\pi^0$ (a), $K^0_S K^\pm\pi^\mp\pi^0\pi^0$ (b), and $K^0_S K^\pm\pi^\mp\pi^+\pi^-$ (c) are seen. The observed peak shapes are not purely Gaussian because of radiation effects and resolution, and for the fit we take shapes from the simulated signal distributions. The sum of two Gaussians describes the shape well. The nonresonant background distribution is described by a second-order polynomial function in this region. We obtain 149 ± 21, 369 ± 32, and 815 ± 31 J/ψ events for the reactions shown in Figs. 16(a)–16(c), respectively. The corresponding results for $\psi(2S)$ events are 23 ± 19, 44 ± 15, and 90 ± 12. Using the results for the number of events, the detection

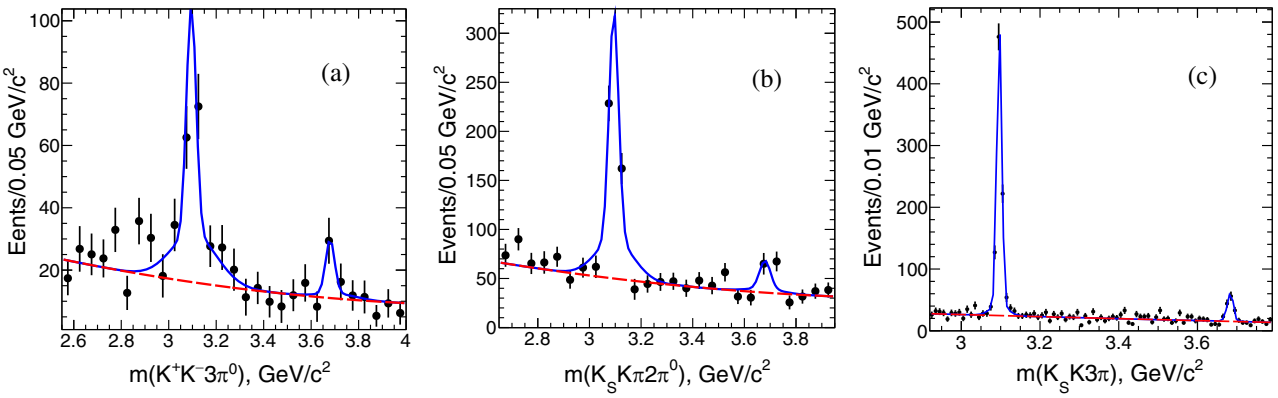

FIG. 16. The J/ψ invariant mass region for the (a) $K^+K^-\pi^0\pi^0\pi^0$, (b) $K^0_S K^\pm\pi^\mp\pi^0\pi^0$, and (c) $K^0_S K^\pm\pi^\mp\pi^+\pi^-$ events. The curves show the fit functions described in the text.

TABLE II. Summary of the J/ψ and $\psi(2S)$ branching fractions. Each value is quoted with its statistical and systematic uncertainties.

		J/ψ or $\psi(2S)$ Branching Fraction (10^{-3})	
Measured Quantity	Measured Value (eV)	Derived, this work	PDG [30]
$\Gamma^{J/\psi}_{ee}\cdot B_{J/\psi\to K^+K^-\pi^0\pi^0\pi^0}$	$8.9\pm1.3\pm0.9$	$1.6\pm0.2\pm0.2$	no entry
$\Gamma^{J/\psi}_{ee}\cdot B_{J/\psi\to\eta K^+K^-}\cdot B_{\eta\to\pi^0\pi^0\pi^0}$	$1.55\pm0.51\pm0.16$	$0.85\pm0.28\pm0.09$	no entry
$\Gamma^{J/\psi}_{ee}\cdot B_{J/\psi\to\phi\eta}\cdot B_{\phi\to K^+K^-}\cdot B_{\eta\to\pi^0\pi^0\pi^0}$	$0.64\pm0.26\pm0.06$	$0.72\pm0.29\pm0.07$	0.74 ± 0.08
$\Gamma^{J/\psi}_{ee}\cdot B_{J/\psi\to K^{*+}K^{*-}\pi^0}\cdot B_{K^{*+}\to K^+\pi^0}\cdot B_{K^{*-}\to K^-\pi^0}$	$6.9\pm1.2\pm0.7$	$5.0\pm0.9\pm0.5$	no entry
$\Gamma^{\psi(2S)}_{ee}\cdot B_{\psi(2S)\to K^+K^-\pi^0\pi^0\pi^0}$	$1.54\pm0.63\pm0.15$	$0.66\pm0.27\pm0.07$	no entry
$\Gamma^{\psi(2S)}_{ee}\cdot B_{\psi(2S)\to J/\psi\pi^0\pi^0}\cdot B_{J/\psi\to K^+K^-\pi^0}$	$1.31\pm0.35\pm0.13$	$3.1\pm0.8\pm0.3$	2.88 ± 0.13
$\Gamma^{\psi(2S)}_{ee}\cdot B_{\psi(2S)\to\eta K^+K^-}\cdot B_{\eta\to\pi^0\pi^0\pi^0}$	<0.2 at 90% C.L.	<0.25 at 90% C.L.	no entry
$\Gamma^{\psi(2S)}_{ee}\cdot B_{\psi(2S)\to K^{*+}K^{*-}\pi^0}\cdot B_{K^{*+}\to K^+\pi^0}\cdot B_{K^{*-}\to K^-\pi^0}$	$0.94\pm0.45\pm0.10$	$1.6\pm0.8\pm0.2$	no entry
$\Gamma^{J/\psi}_{ee}\cdot B_{J/\psi\to K^0_S K^\pm\pi^\mp\pi^0\pi^0}$	$29.3\pm2.6\pm2.9$	$5.3\pm0.5\pm0.5$	no entry
$\Gamma^{J/\psi}_{ee}\cdot B_{J/\psi\to K^{*\pm}K^\mp\pi^0\pi^0}\cdot B_{K^{*\pm}\to K^0\pi^\pm}\cdot B_{K^0\to K^0_S}$	$2.89\pm0.52\pm0.28$	$2.0\pm0.4\pm0.2$	no entry
$\Gamma^{J/\psi}_{ee}\cdot B_{J/\psi\to K^0K^{*0}\pi^0\pi^0}\cdot B_{K^{*0}\to K^\pm\pi^\mp}\cdot B_{K^0\to K^0_S}$	$3.73\pm0.53\pm0.37$	$2.7\pm0.4\pm0.3$	no entry
$\Gamma^{J/\psi}_{ee}\cdot B_{J/\psi\to K^0_S K^\pm\rho^\mp\pi^0}$	$16.0\pm4.1\pm1.6$	$2.9\pm0.7\pm0.3$	no entry
$\Gamma^{\psi(2S)}_{ee}\cdot B_{\psi(2S)\to K^0_S K^\pm\pi^\mp\pi^0\pi^0}$	$4.0\pm1.4\pm0.4$	$1.7\pm0.6\pm0.2$	no entry
$\Gamma^{\psi(2S)}_{ee}\cdot B_{\psi(2S)\to J/\psi\pi^0\pi^0}\cdot B_{J/\psi\to K^0_S K^\pm\pi^\mp}$	$2.36\pm0.59\pm0.24$	$5.5\pm1.4\pm0.6$	5.6 ± 0.5
$\Gamma^{\psi(2S)}_{ee}\cdot B_{\psi(2S)\to K^{*\pm}K^\mp\pi^0\pi^0}\cdot B_{K^{*\pm}\to K^0\pi^\pm}\cdot B_{K^0\to K^0_S}$	$0.54\pm0.22\pm0.05$	$0.92\pm0.37\pm0.09$	no entry
$\Gamma^{\psi(2S)}_{ee}\cdot B_{\psi(2S)\to K^0K^{*0}\pi^0\pi^0}\cdot B_{K^{*0}\to K^\pm\pi^\mp}\cdot B_{K^0\to K^0_S}$	$0.47\pm0.19\pm0.05$	$0.81\pm0.32\pm0.08$	no entry
$\Gamma^{\psi(2S)}_{ee}\cdot B_{\psi(2S)\to K^0_S K^\pm\rho^\mp\pi^0}$	<1.6 at 90% C.L.	<0.6 at 90% C.L.	no entry
$\Gamma^{J/\psi}_{ee}\cdot B_{J/\psi\to K^0_S K^\pm\pi^\mp\pi^+\pi^-}$	$34.6\pm1.4\pm1.8$	$6.2\pm0.2\pm0.4$	no entry
$\Gamma^{J/\psi}_{ee}\cdot B_{J/\psi\to K^{*\pm}K^{*0}\pi^\mp}\cdot B_{K^{*\pm}\to K^0\pi^\pm}\cdot B_{K^{*0}\to K^\pm\pi^\mp}\cdot B_{K^0\to K^0_S}$	$5.9\pm1.0\pm0.6$	$8.5\pm1.5\pm0.9$	no entry
$\Gamma^{J/\psi}_{ee}\cdot B_{J/\psi\to K^{*\pm}K^\mp\pi^+\pi^-}\cdot B_{K^{*\pm}\to K^0\pi^\pm}\cdot B_{K^0\to K^0_S}$	$6.2\pm2.1\pm0.6$	$4.4\pm1.5\pm0.4$	no entry
$\Gamma^{J/\psi}_{ee}\cdot B_{J/\psi\to K^0K^{*0}\pi^+\pi^-}\cdot B_{K^{*0}\to K^\pm\pi^\mp}\cdot B_{K^0\to K^0_S}$	$6.3\pm2.1\pm0.6$	$4.5\pm1.5\pm0.5$	no entry
$\Gamma^{J/\psi}_{ee}\cdot B_{J/\psi\to K^0_S K^\pm\pi^\mp\rho^0}$	$17.3\pm2.1\pm1.7$	$3.1\pm0.4\pm0.3$	no entry
$\Gamma^{\psi(2S)}_{ee}\cdot B_{\psi(2S)\to K^0_S K^\pm\pi^\mp\pi^+\pi^-}$	$5.1\pm0.7\pm0.4$	$2.2\pm0.3\pm0.2$	no entry
$\Gamma^{\psi(2S)}_{ee}\cdot B_{\psi(2S)\to J/\psi\pi^+\pi^-}\cdot B_{J/\psi\to K^0_S K^\pm\pi^\mp}$	$4.14\pm0.55\pm0.29$	$5.1\pm0.7\pm0.1$	5.6 ± 0.5
$\Gamma^{\psi(2S)}_{ee}\cdot B_{\psi(2S)\to K^0_S K^\pm\pi^\mp\rho^0}$	<1.6 at 90% C.L.	<0.6 at 90% C.L.	no entry

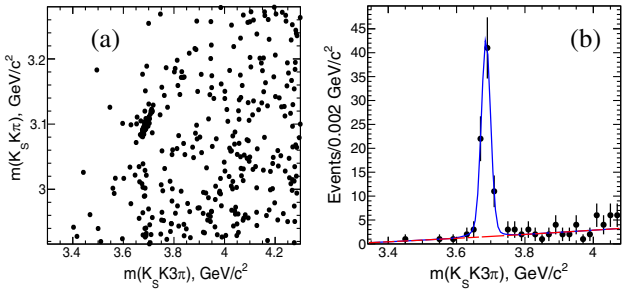

FIG. 17. (a) $m(K^0_S K\pi)$ invariant mass vs $m(K^0_S K3\pi)$ invariant mass for the $K^0_S K^\pm\pi^\mp\pi^+\pi^-$ events around the $\psi(2S)$ signal. (b) $m(K^0_S K3\pi)$ invariant mass distribution with the J/ψ selection in the $K^0_S K^\pm\pi^\mp$ invariant mass. The solid curve shows the fit to the $\psi(2S)$ signal, with a linear background shown by the dashed line.

efficiency, and the ISR luminosity, we determine the product of the decay rate to hadrons and the electronic width:

$$B_{J/\psi\to\mathrm{had}}\cdot\Gamma^{J/\psi}_{ee}=\frac{N(J/\psi\to\mathrm{had})\cdot m^2_{J/\psi}}{6\pi^2\cdot d\mathcal{L}/dE\cdot\epsilon^{\mathrm{MC}}\cdot\epsilon^{\mathrm{corr}}\cdot C}, \quad (2)$$

where $d\mathcal{L}/dE = 180\ \mathrm{nb}^{-1}/\mathrm{MeV}$ is the ISR luminosity at the J/ψ mass $m_{J/\psi}$, ϵ^{MC} is the detection efficiency from simulation with the corrections ϵ^{corr}, discussed in Sec. VI D, and $C = 3.894\times10^{11}\ \mathrm{nb\,MeV}/c^2$ is a conversion constant [30]. We estimate the systematic uncertainty for this region to be 10% according to Table I.

Using $\Gamma^{J/\psi}_{ee} = 5.53\pm0.10$ keV [30], we obtain $B_{J/\psi\to\mathrm{had}}$ for each inclusive final state. The measured products, derived decay rates, and results of previous measurements from the PDG [30] are listed in Table II.

Using Eq. (2) and the result $d\mathcal{L}/dE = 228\ \mathrm{nb}^{-1}/\mathrm{MeV}$ at the $\psi(2S)$ mass, we obtain the products $B_{\psi(2S)\to\mathrm{had}}\cdot\Gamma^{\psi(2S)}_{ee}$ for each decay channel. With $\Gamma^{\psi(2S)}_{ee} = 2.33\pm0.04$ keV [30] we find the corresponding $B_{\psi(2S)\to\mathrm{had}}$ and list them in Table II. These results represent the first measurements for these decay channels.

The observed $\psi(2S)$ signals are partly due to the $\psi(2S)\to J/\psi\pi^+\pi^-, J/\psi\pi^0\pi^0$ transitions. Indeed, if we plot $K^+K^-\pi^0$ or $K^0_S K^\pm\pi^\mp$ invariant masses vs the full hadronic system mass, the J/ψ signal is seen. An example is shown in Fig. 17(a) where the $m(K^0_S K\pi)$ invariant mass is plotted vs the $m(K^0_S K3\pi)$ invariant mass. The $J/\psi\to K^0_S K^\pm\pi^\mp$ decay signal is seen. We select this signal in the $\pm50\ \mathrm{MeV}/c^2$ window around the J/ψ mass and plot the $m(K^0_S K3\pi)$ invariant mass for the selected events, shown in Fig. 17(b) by dots. We fit the $\psi(2S)$ signal with the sum of the Gaussian and linear functions (solid curve) and obtain 73 ± 10 events over the background (dashed curve) for the $\psi(2S)\to J/\psi\pi^+\pi^-, J/\psi\to K^0_S K^\pm\pi^\mp$ transition. A similar study gives 20 ± 5 and 26 ± 6 events for the $\psi(2S)\to J/\psi\pi^0\pi^0, J/\psi\to K^+K^-\pi^0$ and $\psi(2S)\to J/\psi\pi^0\pi^0, J/\psi\to K^0_S K^\pm\pi^\mp$ decay channels, respectively. Using Eq. (2) we calculate the product of the branching fraction and electronic width for each decay chain and list the results in Table II. Because the $\psi(2S)\to J/\psi\pi^+\pi^-, J/\psi\pi^0\pi^0$ transition rates are known with good accuracy, we calculate the J/ψ decay rates and compare them with the direct measurements, presented in the fourth column of Table II [30], and find good agreement.

Because the J/ψ and $\psi(2S)$ signals are narrow with relatively small background, we are able to determine exclusive decay rates that include narrow η, ϕ, K^*, ρ intermediate resonances or correlated production of them. Using event selections for the intermediate structures described in Secs. VII–IX, we extract corresponding numbers of signal events and calculate the product of branching fractions and electronic width. The obtained values are listed in Table II. Using known values for the electronic widths and known decay rates of narrow states, we derive the corresponding branching fractions for the J/ψ and $\psi(2S)$ resonances, listed in the third column of Table II. Almost all of them are measured for the first time.

XI. SUMMARY

The excellent photon-energy and charged-particle momentum resolutions, as well as the particle identification capabilities of the *BABAR* detector, allow the reconstruction of the $K^+K^-\pi^0\pi^0\pi^0$, $K^0_S K^\pm\pi^\mp\pi^0\pi^0$, and $K^0_S K^\pm\pi^\mp\pi^+\pi^-$ final states produced at center-of-mass energies below 4.5 GeV via ISR in data collected at the $\Upsilon(4S)$ center-of-mass region.

The cross sections for the $e^+e^-\to K^+K^-\pi^0\pi^0\pi^0$, $e^+e^-\to K^0_S K^\pm\pi^\mp\pi^0\pi^0$, and $e^+e^-\to K^0_S K^\pm\pi^\mp\pi^+\pi^-$ reactions have been measured for the first time. The accuracy is about 10%. The cross sections for these channels can help to estimate the contribution from the other $K\bar{K}3\pi$ combinations and can improve the reliability of the HVP calculation.

The selected multihadronic final states in the broad range of accessible energies provide new information on hadron spectroscopy. The observed contributions from intermediate narrow η, K^*, and ρ resonances provide additional information for the hadronic contribution calculation of the muon $g_\mu - 2$.

The initial-state radiation events allow a study of J/ψ and $\psi(2S)$ production and a measurement of the corresponding products of the decay branching fractions and e^+e^- width for most of the studied channels, the majority of them for the first time.

TABLE III. Summary of the $e^+e^- \to K^+K^-\pi^0\pi^0\pi^0$ cross section measurement. The uncertainties are statistical only.

$E_{\rm c.m.}$, GeV	σ, nb	$E_{\rm c.m.}$, GeV	σ, nb	$E_{\rm c.m.}$, GeV	σ, nb	$E_{\rm c.m.}$, GeV	σ, nb	$E_{\rm c.m.}$, GeV	σ, nb
1.525	0.03 ± 0.03	2.125	0.14 ± 0.04	2.725	0.08 ± 0.02	3.325	0.03 ± 0.02	3.925	0.02 ± 0.01
1.575	0.16 ± 0.05	2.175	0.09 ± 0.03	2.775	0.10 ± 0.03	3.375	0.04 ± 0.01	3.975	0.01 ± 0.01
1.625	0.36 ± 0.07	2.225	0.03 ± 0.03	2.825	0.04 ± 0.02	3.425	0.02 ± 0.02	4.025	0.03 ± 0.01
1.675	0.45 ± 0.07	2.275	0.09 ± 0.03	2.875	0.11 ± 0.03	3.475	0.02 ± 0.02	4.075	0.02 ± 0.01
1.725	0.38 ± 0.06	2.325	0.05 ± 0.03	2.925	0.09 ± 0.02	3.525	0.03 ± 0.02	4.125	0.03 ± 0.01
1.775	0.29 ± 0.05	2.375	0.08 ± 0.03	2.975	0.05 ± 0.02	3.575	0.04 ± 0.02	4.175	0.02 ± 0.01
1.825	0.21 ± 0.05	2.425	0.06 ± 0.02	3.025	0.10 ± 0.03	3.625	0.02 ± 0.01	4.225	0.01 ± 0.01
1.875	0.21 ± 0.05	2.475	0.12 ± 0.03	3.075	0.18 ± 0.03	3.675	0.07 ± 0.02	4.275	0.01 ± 0.01
1.925	0.17 ± 0.03	2.525	0.07 ± 0.02	3.125	0.21 ± 0.03	3.725	0.04 ± 0.02	4.325	0.02 ± 0.01
1.975	0.09 ± 0.03	2.575	0.06 ± 0.02	3.175	0.08 ± 0.02	3.775	0.03 ± 0.01	4.375	0.03 ± 0.01
2.025	0.09 ± 0.03	2.625	0.09 ± 0.03	3.225	0.08 ± 0.02	3.825	0.02 ± 0.01	4.425	0.01 ± 0.01
2.075	0.21 ± 0.04	2.675	0.09 ± 0.03	3.275	0.05 ± 0.02	3.875	0.01 ± 0.01	4.475	0.01 ± 0.01

TABLE IV. Summary of the $e^+e^- \to K^0_S K^\pm\pi^\mp\pi^0\pi^0$ cross section measurement. The uncertainties are statistical only.

$E_{\rm c.m.}$, GeV	σ, nb	$E_{\rm c.m.}$, GeV	σ, nb	$E_{\rm c.m.}$, GeV	σ, nb	$E_{\rm c.m.}$, GeV	σ, nb	$E_{\rm c.m.}$, GeV	σ, nb
1.875	0.00 ± 0.01	2.425	0.34 ± 0.06	2.975	0.25 ± 0.05	3.525	0.19 ± 0.04	4.075	0.09 ± 0.02
1.925	0.01 ± 0.03	2.475	0.42 ± 0.07	3.025	0.25 ± 0.05	3.575	0.10 ± 0.03	4.125	0.04 ± 0.02
1.975	0.01 ± 0.03	2.525	0.40 ± 0.06	3.075	0.95 ± 0.08	3.625	0.10 ± 0.03	4.175	0.05 ± 0.02
2.025	0.05 ± 0.03	2.575	0.30 ± 0.05	3.125	0.67 ± 0.07	3.675	0.20 ± 0.04	4.225	0.07 ± 0.02
2.075	0.14 ± 0.05	2.625	0.29 ± 0.06	3.175	0.14 ± 0.05	3.725	0.19 ± 0.04	4.275	0.03 ± 0.02
2.125	0.15 ± 0.05	2.675	0.36 ± 0.06	3.225	0.14 ± 0.04	3.775	0.06 ± 0.03	4.325	0.01 ± 0.02
2.175	0.30 ± 0.06	2.725	0.41 ± 0.06	3.275	0.18 ± 0.04	3.825	0.09 ± 0.03	4.375	0.06 ± 0.02
2.225	0.31 ± 0.07	2.775	0.27 ± 0.05	3.325	0.15 ± 0.04	3.875	0.09 ± 0.03	4.425	0.05 ± 0.02
2.275	0.24 ± 0.05	2.825	0.28 ± 0.06	3.375	0.13 ± 0.04	3.925	0.10 ± 0.03	4.475	0.04 ± 0.02
2.325	0.28 ± 0.06	2.875	0.29 ± 0.05	3.425	0.16 ± 0.03	3.975	0.08 ± 0.03		
2.375	0.34 ± 0.06	2.925	0.19 ± 0.04	3.475	0.13 ± 0.04	4.025	0.07 ± 0.03		

TABLE V. Summary of the $e^+e^- \to K^0_S K^\pm\pi^\mp\pi^+\pi^-$ cross section measurement. The uncertainties are statistical only.

$E_{\rm c.m.}$, GeV	σ, nb	$E_{\rm c.m.}$, GeV	σ, nb	$E_{\rm c.m.}$, GeV	σ, nb	$E_{\rm c.m.}$, GeV	σ, nb	$E_{\rm c.m.}$, GeV	σ, nb
1.775	0.01 ± 0.01	2.325	0.38 ± 0.04	2.875	0.23 ± 0.03	3.425	0.18 ± 0.02	3.975	0.09 ± 0.02
1.825	0.01 ± 0.01	2.375	0.38 ± 0.04	2.925	0.28 ± 0.03	3.475	0.18 ± 0.02	4.025	0.07 ± 0.02
1.875	0.02 ± 0.01	2.425	0.48 ± 0.04	2.975	0.21 ± 0.03	3.525	0.15 ± 0.02	4.075	0.12 ± 0.02
1.925	0.02 ± 0.01	2.475	0.34 ± 0.04	3.025	0.21 ± 0.03	3.575	0.14 ± 0.02	4.125	0.08 ± 0.02
1.975	0.07 ± 0.02	2.525	0.37 ± 0.03	3.075	1.44 ± 0.06	3.625	0.11 ± 0.02	4.175	0.07 ± 0.01
2.025	0.10 ± 0.02	2.575	0.30 ± 0.03	3.125	0.69 ± 0.05	3.675	0.30 ± 0.03	4.225	0.07 ± 0.01
2.075	0.16 ± 0.03	2.625	0.32 ± 0.04	3.175	0.21 ± 0.03	3.725	0.08 ± 0.02	4.275	0.09 ± 0.02
2.125	0.28 ± 0.03	2.675	0.33 ± 0.03	3.225	0.17 ± 0.03	3.775	0.11 ± 0.02	4.325	0.05 ± 0.02
2.175	0.40 ± 0.04	2.725	0.33 ± 0.03	3.275	0.20 ± 0.03	3.825	0.12 ± 0.02	4.375	0.06 ± 0.02
2.225	0.31 ± 0.04	2.775	0.31 ± 0.03	3.325	0.15 ± 0.02	3.875	0.10 ± 0.02	4.425	0.06 ± 0.01
2.275	0.30 ± 0.03	2.825	0.22 ± 0.03	3.375	0.15 ± 0.02	3.925	0.09 ± 0.02	4.475	0.03 ± 0.01

TABLE VI. Summary of the $e^+e^- \to K^+K^-\eta$ cross section measurement. The uncertainties are statistical only.

$E_{\rm c.m.}$, GeV	σ, nb	$E_{\rm c.m.}$, GeV	σ, nb	$E_{\rm c.m.}$, GeV	σ, nb	$E_{\rm c.m.}$, GeV	σ, nb	$E_{\rm c.m.}$, GeV	σ, nb
1.525	0.00 ± 0.04	1.925	0.24 ± 0.09	2.325	0.01 ± 0.02	2.725	0.03 ± 0.03	3.125	0.06 ± 0.03
1.575	0.09 ± 0.12	1.975	0.12 ± 0.07	2.375	0.03 ± 0.04	2.775	0.03 ± 0.02	3.175	0.00 ± 0.01
1.625	1.17 ± 0.23	2.025	0.21 ± 0.08	2.425	0.02 ± 0.04	2.825	0.04 ± 0.03	3.225	0.02 ± 0.02
1.675	1.47 ± 0.25	2.075	0.22 ± 0.08	2.475	0.06 ± 0.05	2.875	0.00 ± 0.01	3.275	0.00 ± 0.01
1.725	1.39 ± 0.21	2.125	0.21 ± 0.08	2.525	0.07 ± 0.04	2.925	0.01 ± 0.01	3.325	0.01 ± 0.02
1.775	0.78 ± 0.18	2.175	0.17 ± 0.06	2.575	0.08 ± 0.04	2.975	0.00 ± 0.02	3.375	0.01 ± 0.02
1.825	0.55 ± 0.14	2.225	0.04 ± 0.04	2.625	0.04 ± 0.04	3.025	0.03 ± 0.03	3.425	0.01 ± 0.01
1.875	0.56 ± 0.14	2.275	0.15 ± 0.05	2.675	0.06 ± 0.03	3.075	0.15 ± 0.05	3.475	0.00 ± 0.01

TABLE VII. Summary of the $e^+e^- \to \phi(1020)\eta$ cross section measurement. The uncertainties are statistical only.

$E_{\text{c.m.}}$, GeV	σ, nb	$E_{\text{c.m.}}$, GeV	σ, nb	$E_{\text{c.m.}}$, GeV	σ, nb	$E_{\text{c.m.}}$, GeV	σ, nb	$E_{\text{c.m.}}$, GeV	σ, nb
1.525	0.00 ± 0.09	1.875	1.12 ± 0.23	2.225	0.11 ± 0.07	2.575	0.11 ± 0.05	2.925	0.01 ± 0.03
1.575	0.27 ± 0.25	1.925	0.42 ± 0.14	2.275	0.25 ± 0.08	2.625	0.05 ± 0.04	2.975	0.02 ± 0.03
1.625	2.24 ± 0.44	1.975	0.22 ± 0.11	2.325	0.02 ± 0.03	2.675	0.11 ± 0.05	3.025	0.04 ± 0.03
1.675	2.87 ± 0.47	2.025	0.33 ± 0.11	2.375	0.10 ± 0.05	2.725	0.06 ± 0.04	3.075	0.17 ± 0.06
1.725	2.36 ± 0.40	2.075	0.37 ± 0.11	2.425	0.12 ± 0.06	2.775	0.04 ± 0.03	3.125	0.03 ± 0.03
1.775	1.54 ± 0.30	2.125	0.32 ± 0.11	2.475	0.14 ± 0.06	2.825	0.02 ± 0.02	3.175	0.00 ± 0.01
1.825	0.82 ± 0.22	2.175	0.26 ± 0.09	2.525	0.07 ± 0.05	2.875	0.00 ± 0.01	3.225	0.04 ± 0.03

TABLE VIII. Summary of the $e^+e^- \to K^{*+}K^{*-}\pi^0$ cross section measurement. The uncertainties are statistical only.

$E_{\text{c.m.}}$, GeV	σ, nb	$E_{\text{c.m.}}$, GeV	σ, nb	$E_{\text{c.m.}}$, GeV	σ, nb	$E_{\text{c.m.}}$, GeV	σ, nb	$E_{\text{c.m.}}$, GeV	σ, nb
1.875	0.00 ± 0.05	2.425	0.24 ± 0.10	2.975	0.29 ± 0.08	3.525	0.20 ± 0.05	4.075	0.07 ± 0.03
1.925	0.03 ± 0.05	2.475	0.39 ± 0.11	3.025	0.17 ± 0.09	3.575	0.13 ± 0.05	4.125	0.06 ± 0.03
1.975	0.06 ± 0.05	2.525	0.32 ± 0.10	3.075	0.90 ± 0.13	3.625	0.10 ± 0.05	4.175	0.06 ± 0.03
2.025	0.16 ± 0.07	2.575	0.39 ± 0.10	3.125	0.37 ± 0.10	3.675	0.22 ± 0.06	4.225	0.08 ± 0.03
2.075	0.07 ± 0.12	2.625	0.38 ± 0.10	3.175	0.24 ± 0.07	3.725	0.17 ± 0.05	4.275	0.08 ± 0.03
2.125	0.41 ± 0.19	2.675	0.20 ± 0.10	3.225	0.20 ± 0.07	3.775	0.06 ± 0.04	4.325	0.01 ± 0.02
2.175	0.29 ± 0.09	2.725	0.22 ± 0.09	3.275	0.19 ± 0.06	3.825	0.12 ± 0.04	4.375	0.05 ± 0.03
2.225	0.16 ± 0.09	2.775	0.24 ± 0.09	3.325	0.10 ± 0.05	3.875	0.08 ± 0.03	4.425	0.04 ± 0.03
2.275	0.31 ± 0.15	2.825	0.16 ± 0.07	3.375	0.06 ± 0.05	3.925	0.13 ± 0.04	4.475	0.05 ± 0.03
2.325	0.17 ± 0.09	2.875	0.26 ± 0.08	3.425	0.07 ± 0.05	3.975	0.02 ± 0.03		
2.375	0.45 ± 0.18	2.925	0.33 ± 0.10	3.475	0.10 ± 0.05	4.025	0.04 ± 0.03		

TABLE IX. Summary of the $e^+e^- \to K^0_S K^*(892)^0\pi^0\pi^0$ cross section measurement. The uncertainties are statistical only.

$E_{\text{c.m.}}$, GeV	σ, nb	$E_{\text{c.m.}}$, GeV	σ, nb	$E_{\text{c.m.}}$, GeV	σ, nb	$E_{\text{c.m.}}$, GeV	σ, nb	$E_{\text{c.m.}}$, GeV	σ, nb
1.875	0.01 ± 0.04	2.425	0.25 ± 0.09	2.975	0.13 ± 0.07	3.525	0.04 ± 0.03	4.075	0.05 ± 0.03
1.925	0.02 ± 0.04	2.475	0.17 ± 0.09	3.025	0.06 ± 0.05	3.575	0.01 ± 0.02	4.125	0.02 ± 0.02
1.975	0.01 ± 0.04	2.525	0.31 ± 0.10	3.075	0.38 ± 0.12	3.625	0.04 ± 0.03	4.175	0.02 ± 0.02
2.025	0.01 ± 0.04	2.575	0.18 ± 0.06	3.125	0.36 ± 0.09	3.675	0.11 ± 0.05	4.225	0.02 ± 0.02
2.075	0.11 ± 0.07	2.625	0.06 ± 0.05	3.175	0.05 ± 0.04	3.725	0.01 ± 0.02	4.275	0.01 ± 0.01
2.125	0.06 ± 0.05	2.675	0.09 ± 0.06	3.225	0.09 ± 0.05	3.775	0.01 ± 0.02	4.325	0.02 ± 0.02
2.175	0.21 ± 0.10	2.725	0.13 ± 0.07	3.275	0.04 ± 0.04	3.825	0.07 ± 0.03	4.375	0.02 ± 0.02
2.225	0.44 ± 0.11	2.775	0.17 ± 0.08	3.325	0.09 ± 0.05	3.875	0.04 ± 0.03	4.425	0.01 ± 0.02
2.275	0.32 ± 0.09	2.825	0.10 ± 0.06	3.375	0.06 ± 0.04	3.925	0.03 ± 0.02	4.475	0.01 ± 0.01
2.325	0.23 ± 0.09	2.875	0.12 ± 0.07	3.425	0.03 ± 0.03	3.975	0.02 ± 0.02		
2.375	0.28 ± 0.10	2.925	0.15 ± 0.07	3.475	0.08 ± 0.04	4.025	0.00 ± 0.02		

TABLE X. Summary of the $e^+e^- \to K^*(892)^{\pm}K^{\mp}\pi^0\pi^0$ cross section measurement. The uncertainties are statistical only.

$E_{\text{c.m.}}$, GeV	σ, nb	$E_{\text{c.m.}}$, GeV	σ, nb	$E_{\text{c.m.}}$, GeV	σ, nb	$E_{\text{c.m.}}$, GeV	σ, nb	$E_{\text{c.m.}}$, GeV	σ, nb
1.925	0.00 ± 0.04	2.475	0.13 ± 0.10	3.025	0.16 ± 0.08	3.575	0.06 ± 0.04	4.125	0.06 ± 0.03
1.975	0.02 ± 0.03	2.525	0.14 ± 0.10	3.075	0.37 ± 0.11	3.625	0.03 ± 0.03	4.175	0.02 ± 0.02
2.025	0.09 ± 0.06	2.575	0.17 ± 0.08	3.125	0.25 ± 0.08	3.675	0.12 ± 0.04	4.225	0.06 ± 0.03
2.075	0.07 ± 0.04	2.625	0.14 ± 0.07	3.175	0.19 ± 0.06	3.725	0.08 ± 0.05	4.275	0.03 ± 0.02
2.125	0.13 ± 0.07	2.675	0.14 ± 0.08	3.225	0.08 ± 0.05	3.775	0.03 ± 0.03	4.325	0.00 ± 0.02
2.175	0.20 ± 0.10	2.725	0.22 ± 0.10	3.275	0.04 ± 0.04	3.825	0.06 ± 0.02	4.375	0.07 ± 0.02
2.225	0.28 ± 0.10	2.775	0.17 ± 0.08	3.325	0.13 ± 0.05	3.875	0.05 ± 0.03	4.425	0.03 ± 0.02
2.275	0.17 ± 0.07	2.825	0.26 ± 0.08	3.375	0.09 ± 0.04	3.925	0.00 ± 0.02	4.475	0.03 ± 0.02
2.325	0.18 ± 0.09	2.875	0.12 ± 0.07	3.425	0.03 ± 0.03	3.975	0.03 ± 0.03		
2.375	0.13 ± 0.10	2.925	0.23 ± 0.07	3.475	0.03 ± 0.03	4.025	0.00 ± 0.02		
2.425	0.19 ± 0.09	2.975	0.10 ± 0.06	3.525	0.10 ± 0.05	4.075	0.02 ± 0.02		

TABLE XI. Summary of the $e^+e^- \to K^0_S K^\pm \rho^\mp \pi^0$ cross section measurement. The uncertainties are statistical only.

$E_{\mathrm{c.m.}}$, GeV	σ, nb	$E_{\mathrm{c.m.}}$, GeV	σ, nb	$E_{\mathrm{c.m.}}$, GeV	σ, nb	$E_{\mathrm{c.m.}}$, GeV	σ, nb	$E_{\mathrm{c.m.}}$, GeV	σ, nb
2.225	0.00 ± 0.01	2.675	0.33 ± 0.08	3.125	0.40 ± 0.09	3.575	0.08 ± 0.04	4.025	0.06 ± 0.03
2.275	0.03 ± 0.06	2.725	0.22 ± 0.07	3.175	0.16 ± 0.06	3.625	0.10 ± 0.04	4.075	0.06 ± 0.03
2.325	0.13 ± 0.07	2.775	0.16 ± 0.07	3.225	0.10 ± 0.05	3.675	0.06 ± 0.05	4.125	0.04 ± 0.03
2.375	0.06 ± 0.07	2.825	0.12 ± 0.06	3.275	0.22 ± 0.06	3.725	0.17 ± 0.05	4.175	0.05 ± 0.03
2.425	0.22 ± 0.08	2.875	0.16 ± 0.07	3.325	0.17 ± 0.05	3.775	0.06 ± 0.03	4.225	0.01 ± 0.03
2.475	0.18 ± 0.08	2.925	0.20 ± 0.07	3.375	0.06 ± 0.04	3.825	0.07 ± 0.04	4.275	0.02 ± 0.02
2.525	0.27 ± 0.08	2.975	0.23 ± 0.07	3.425	0.16 ± 0.05	3.875	0.07 ± 0.03	4.325	0.04 ± 0.02
2.575	0.15 ± 0.07	3.025	0.15 ± 0.07	3.475	0.11 ± 0.04	3.925	0.05 ± 0.03	4.375	0.07 ± 0.03
2.625	0.26 ± 0.07	3.075	0.51 ± 0.10	3.525	0.11 ± 0.05	3.975	0.03 ± 0.03	4.425	0.03 ± 0.02

TABLE XII. Summary of the $e^+e^- \to f_1(1285)\pi^+\pi^-$ cross section measurement. The uncertainties are statistical only.

$E_{\mathrm{c.m.}}$, GeV	σ, nb	$E_{\mathrm{c.m.}}$, GeV	σ, nb	$E_{\mathrm{c.m.}}$, GeV	σ, nb	$E_{\mathrm{c.m.}}$, GeV	σ, nb	$E_{\mathrm{c.m.}}$, GeV	σ, nb
1.650	0.02 ± 0.09	2.250	0.48 ± 0.27	2.850	0.02 ± 0.09	3.450	0.21 ± 0.09	4.050	0.09 ± 0.06
1.750	0.30 ± 0.16	2.350	0.20 ± 0.19	2.950	0.20 ± 0.12	3.550	0.05 ± 0.06	4.150	0.04 ± 0.05
1.850	0.28 ± 0.18	2.450	0.49 ± 0.25	3.050	0.03 ± 0.06	3.650	0.08 ± 0.09	4.250	0.02 ± 0.05
1.950	0.90 ± 0.26	2.550	0.11 ± 0.16	3.150	0.15 ± 0.09	3.750	0.12 ± 0.12	4.350	0.00 ± 0.05
2.050	0.84 ± 0.28	2.650	0.12 ± 0.15	3.250	0.06 ± 0.08	3.850	0.00 ± 0.09	4.450	0.00 ± 0.05
2.150	0.97 ± 0.32	2.750	0.06 ± 0.12	3.350	0.02 ± 0.05	3.950	0.15 ± 0.09	4.550	0.00 ± 0.00

ACKNOWLEDGMENTS

We are grateful for the extraordinary contributions of our PEP-II colleagues in achieving the excellent luminosity and machine conditions that have made this work possible. The success of this project also relies critically on the expertise and dedication of the computing organizations that support *BABAR*. The collaborating institutions wish to thank SLAC for its support and the kind hospitality extended to them. We also wish to acknowledge the important contributions of J. Dorfan, W. Dunwoodie, and our deceased colleagues E. Gabathuler, W. Innes, D. W. G. S. Leith, A. Onuchin, G. Piredda, and R. F. Schwitters.

[1] M. Davier, A. Hoecker, B. Malaescu, and Z. Zhang, Eur. Phys. J. C **77**, 827 (2017); Fred Jegerlehner, EPJ Web Conf. **166**, 00022 (2018); A. Keshavarzi, D. Nomura, and T. Teubner, Phys. Rev. D **97**, 114025 (2018).
[2] T. Aoyama *et al.*, Phys. Rep. **887**, 1 (2020).
[3] B. Abi *et al.*, Phys. Rev. Lett. **126**, 141801 (2021).
[4] V. N. Baier and V. S. Fadin, Phys. Lett. **27B**, 223 (1968).
[5] A. B. Arbuzov, E. A. Kuraev, N. P. Merenkov, and L. Trentadue, J. High Energy Phys. 12 (1998) 009.
[6] S. Binner, J. H. Kühn, and K. Melnikov, Phys. Lett. B **459**, 279 (1999).
[7] M. Benayoun, S. I. Eidelman, V. N. Ivanchenko, and Z. K. Silagadze, Mod. Phys. Lett. A **14**, 2605 (1999).
[8] B. Aubert *et al.* (*BABAR* Collaboration), Phys. Rev. D **69**, 011103 (2004).
[9] B. Aubert *et al.* (*BABAR* Collaboration), Phys. Rev. D **70**, 072004 (2004).
[10] B. Aubert *et al.* (*BABAR* Collaboration), Phys. Rev. D **71**, 052001 (2005).
[11] B. Aubert *et al.* (*BABAR* Collaboration), Phys. Rev. D **73**, 052003 (2006).
[12] B. Aubert *et al.* (*BABAR* Collaboration), Phys. Rev. D **76**, 092005 (2007).
[13] B. Aubert *et al.* (*BABAR* Collaboration), Phys. Rev. D **77**, 092002 (2008).
[14] B. Aubert *et al.* (*BABAR* Collaboration), Phys. Rev. Lett. **103**, 231801 (2009); J. P. Lees *et al.* (*BABAR* Collaboration), Phys. Rev. D **86**, 032013 (2012).
[15] B. Aubert *et al.* (*BABAR* Collaboration), Phys. Rev. D **86**, 012008 (2012).
[16] J. P. Lees *et al.* (*BABAR* Collaboration), Phys. Rev. D **88**, 032013 (2013).
[17] J. P. Lees *et al.* (*BABAR* Collaboration), Phys. Rev. D **88**, 072009 (2013).
[18] J. P. Lees *et al.* (*BABAR* Collaboration), Phys. Rev. D **89**, 092002 (2014).
[19] J. P. Lees *et al.* (*BABAR* Collaboration), Phys. Rev. D **96**, 092007 (2017).

[20] J. P. Lees *et al.* (*BABAR* Collaboration), Phys. Rev. D **98**, 112015 (2018).
[21] J. P. Lees *et al.* (*BABAR* Collaboration), Phys. Rev. D **97**, 052007 (2018).
[22] J. P. Lees *et al.* (*BABAR* Collaboration), Phys. Rev. D **103**, 092001 (2021).
[23] J. P. Lees *et al.* (*BABAR* Collaboration), Phys. Rev. D **104**, 112004 (2021).
[24] J. P. Lees *et al.* (*BABAR* Collaboration), Nucl. Instrum. Methods Phys. Res., Sect. A **726**, 203 (2013).
[25] B. Aubert *et al.* (*BABAR* Collaboration), Nucl. Instrum. Methods Phys. Res., Sect. A **479**, 1 (2002); **729**, 615 (2013).
[26] H. Czyż and J. H. Kühn, Eur. Phys. J. C **18**, 497 (2001).
[27] A. B. Arbuzov, E. A. Kuraev, G. V. Fedotovich, N. P. Merenkov, V. D. Rushai, and L. Trentadue, J. High Energy Phys. 10 (1997) 001.
[28] M. Caffo, H. Czyż, and E. Remiddi, Nuovo Cimento A **110**, 515 (1997); Phys. Lett. B **327**, 369 (1994).
[29] E. Barberio, B. van Eijk, and Z. Was, Comput. Phys. Commun. **66**, 115 (1991).
[30] P. A. Zyla *et al.* (Particle Data Group), Prog. Theor. Exp. Phys. **2020**, 083C01 (2020).
[31] S. Agostinelli *et al.* (GEANT4 Collaboration), Nucl. Instrum. Methods Phys. Res., Sect. A **506**, 250 (2003).
[32] T. Sjöstrand, Comput. Phys. Commun. **82**, 74 (1994).
[33] S. Jadach and Z. Was, Comput. Phys. Commun. **85**, 453 (1995).
[34] R. R. Ahmetshin *et al.* (CMD3 Collaboration), Phys. Lett. B **798**, 134946 (2019).
[35] C. P. Shen *et al.* (Belle Collaboration), Phys. Rev. D **80**, 031101(R) (2009).
[36] C. P. Shen and C. Z. Yuan, Chin. Phys. C **34**, 1045 (2010).